HHS Public Access

Author manuscript

Nano Res. Author manuscript; available in PMC 2021 July 30.

Published in final edited form as:

Nano Res. 2020 May ; 13(5): 1281–1294. doi:10.1007/s12274-020-2721-0.

A mini-review on rare-earth down-conversion nanoparticles for NIR-II imaging of biological systems

Yeteng Zhong, **Hongjie Dai**

Department of Chemistry, Stanford University, Stanford, California 94305, USA

Abstract

Rare-earth (RE) based luminescent probes exhibit rich optical properties including upconversion and down-conversion luminescence spanning a broad spectral range from 300 to 3,000 nm, and have generated great scientific and practical interest from telecommunication to biological imaging. While upconversion nanoparticles have been investigated for decades, down-conversion luminescence of RE-based probes in the second near-infrared (NIR-II, 1,000–1,700 nm) window for *in vivo* biological imaging with sub-centimeter tissue penetration and micrometer image resolution has come into light only recently. In this review, we present recent progress on RE-based NIR-II probes for *in vivo* vasculature and molecular imaging with a focus on Er^{3+}-based nanoparticles due to the down-conversion luminescence at the long-wavelength end of the NIR-II window (NIR-IIb, 1,500–1,700 nm). Imaging in NIR-IIb is superior to imaging with organic probes such as ICG and IRDye800 in the ~ 800 nm NIR range and the 1,000–1,300 nm short end of NIR-II range, owing to minimized light scattering and autofluorescence background. Doping by cerium and other ions and phase engineering of Er^{3+}-based nanoparticles, combined with surface hydrophilic coating optimization can afford ultrabright, biocompatible NIR-IIb probe towards clinical translation for human use. The Nd^{3+}-based probes with NIR-II emission at 1,050 and 1,330 nm are also discussed, including Nd^{3+} doped nanocrystals and Nd^{3+}-organic ligand complexes. This review also points out future directions for further development of multi-functional RE NIR-II probes for biological imaging.

Keywords

rare earth; down-conversion; near-infrared; biological imaging

1 Introduction

In vivo photoluminescence bio-imaging by collecting emitted light within the body of living animals, instead of cultured cells or anatomical tissues, allows visualization of biological structures, functions and processes with high spatial and temporal resolutions exceeding those of other imaging modalities based on magnetic resonance, X-ray or positron emissions [1–3]. For decades, one-photon *in vivo* optical imaging techniques detecting light emission in the visible (400–700 nm) and traditional near-infrared (NIR-I; 700–900 nm) windows are challenging due to strong autofluorescence and high light-scattering coefficient of live

Address correspondence to hdai1@stanford.edu.

tissues, lowering imaging clarity and degrading signal to background contrasts. Since the pioneering work of our group on detecting the intrinsic photoluminescence of single-walled carbon nanotubes (CNT) circulating in mice vasculatures [4], the past ten years have witnessed significant research activities in the field of *in vivo* optical imaging in the second near-infrared (NIR-II; 1,000–1,700 nm) window, accompanied by the development of fluorescent or luminescent probes based on a wide range of materials including small molecules [5–9], CNTs [10–14], polymer-encapsulated organic dyes [15, 16], inorganic quantum dots (QDs) and nanoparticles [17–22]. Within 1,000–1,700 nm range, 1,300–1,400 nm is called the NIR-IIa window [10] and 1,500–1,700 nm is called the NIR-IIb window [23], and the two sub-windows were separated by a water overtone absorption peak at ~ 1,450 nm [1]. NIR-II imaging is now well established to afford high-resolution micrometer scale imaging at sub-centimeter tissue depths, taking advantage of suppressed light-scattering and diminished tissue autofluorescence in the 1,000–1,700 nm spectral range. In particular, imaging in the NIR-IIb range can maximize the benefit of NIR-II imaging and is superior to imaging in the 1,000–1,300 nm range.

Various classes of NIR-II probes have been developed for NIR-II imaging of mice disease models *in vivo*, with continuously improved functionality and versatility aimed at visualization of molecular and cellular scale biological processes in a living body and for facilitating molecularly targeted diagnosis and therapies [24–30]. Among these NIR-II emitting materials, rare earth (RE) based NIR-II luminescent probe is one of the most promising agents due to its unique luminescence properties in the NIR-II spectral region including narrow-band emission and superior photostability, and the intrinsic low-toxicity of lanthanide elements required for biocompatibility [31]. Further, the recently developed layer-by-layer cross-linked coating on RE nanoparticles enabled rapid excretion after administration and imaging [32], making this class of materials potentially useful for clinical translation for human use. Although RE nanoparticles with interesting upconversion luminescence in the visible range have been investigated for several decades, research on down-conversion NIR-II emitting RE nanoparticles are still in its infancy.

In terms of size, NIR-II luminescent RE compounds mainly fall into two categories. The first is inorganic nanoparticle with lanthanide dopants embedded in the lattice of a host nanocrystal. Generally, a nano-size less than 50 nm is preferred for these nanoparticles to maximize their permeation ability through tissues, organ and tumor [33]. However, the small nano-size is a negative factor for the emission intensity of RE probes, since the decrease in nanocrystal size is usually accompanied by generating of both surface and interior defects, resulting in reduced lanthanide luminescence. Another important requirement of RE nanocrystals for NIR-II imaging is hydrophilic polymer coating for dispersity in aqueous solutions and high biocompatibility and stability in complex physiological environments to minimize toxicity and side-effects. This is very important since most RE nanoparticles are synthesized in oil like organic solvents with hydrophobic capping layers, and must be replaced or over-coated by hydrophilic layers to impart biocompatibility.

The second type of compound is small molecule RE complexes containing RE metal ions coordinated with organic ligands. Such molecules can be excreted rapidly through urine and hold high potential for translation of NIR-II luminescent agents into the clinic. Indeed, a

total of 11 gadolinium-organic ligand complexes have been approved by the FDA as contrast agents for magnetic resonance imaging (MRI) and are used in the clinic [34]. Although versatile organic ligands and various lanthanide ions could allow for the design of a series of RE complexes for high NIR-II luminescence efficiency, another challenge is the luminescence quenching problem in aqueous solutions. When the lanthanide ions are in close proximity to water molecules, quenching can occur caused by strong interactions between the lanthanide ion and abundant hydroxyl groups surrounding the RE complexes in aqueous biological environments [35–37].

Significant effort has been taken in recent years to boost the down-conversion luminescence intensity and optimize the biological compatibility of NIR-II luminescent RE compounds for improved capacity of high-quality *in vivo* imaging. This mini review is not intended to provide a comprehensive survey of all aspects of photoluminescence bio-imaging with lanthanide agents, but instead focuses on the recent progress in RE based NIR-II luminescent probes and their applications in optical *in vivo* bio-imaging/analysis techniques.

2 Optical properties of RE based NIR-II luminescent probes

One of the most interesting features of trivalent RE ions is their unique 4f–4f photoluminescence spanning a wide spectrum from ultraviolet to visible and near-infrared ranges [38–40]. For RE^{3+} ions having a partly filled 4f shell, the electronic configurations are given by

$$(\mathrm{Pd\,core})\,4f^{n}\,5s^{2}\,5p^{6}$$

where n varies from 1 to 13 when going from Ce to Yb [41]. The electric-dipole transitions between 4f levels are responsible for the rich variety of optical absorption and emission lines in the spectra of RE^{3+} ions [39]. According to the quantum mechanical selection rules these electric-dipole 4f–4f transition are parity forbidden, since the $4f^{n}$ configurations in free ions have the same parity [42]. However, when the RE ion is in a site which lacks inversion symmetry, such prohibition can be partially broken through a slight admixture of opposite-parity states of the $4f^{(n-1)}5d$ or $4f^{(n-1)}5g$ configuration into the $4f^{n}$ states by an odd-parity crystal field component [43]. A lower-symmetry lattice can facilitate this mixing of opposite parity configurations, resulting in luminescence enhancement of the RE^{3+} ions [44]. The effect of this mixing on the selection rules was investigated independently by Judd and Ofelt, well known as the Judd-Ofelt theory [45, 46]. On the other hand, the outer 5s and 5p shells of trivalent lanthanide ion can shield the inner 4f shell from the perturbation of surrounding environment, imparting lanthanide ions with specific luminescent properties such as narrow-band emission and long lifetimes of the excited states [38]. Moreover, such shielding effects lead to well-defined 4f energy levels and corresponding absorption & emission spectral lines of RE^{3+} ion with almost no variation in different chemical environments, enabled the engineering of rare-earth based luminescent probes by doping of RE^{3+} ions in a variety of host materials.

The emission and absorption wavelength of a lanthanide ion depends on its energy levels and energy transitions between these levels, while the luminescence by the RE ion is only

possible from certain levels, which are termed resonance levels. Usually when the lanthanide ion is excited to a certain energy level, part of the excitation energy will be dissipated via nonradiative processes until a resonance level is reached for the generating of luminescence. The emitted photon has less energy (longer wavelength) than the absorbed photon, which is the so-called Stokes shift and gives the down-conversion luminescence (Fig. 1(a)). In certain circumstances, anti-Stokes shift may occur when the lanthanide ion is pumped to a higher energy level through multiple photon absorption processes, allowing generation of luminescence with higher photon energy (shorter wavelength) than the excitation light. This phenomenon is well-known as the upconversion luminescence (Fig. 1(a)). Among the 15 rare-earth elements, Pr^{3+}, Nd^{3+}, Ho^{3+}, Er^{3+}, Tm^{3+} are of great interest and potential for the NIR-II down-conversion luminescent probes due to their emission lines in the spectral range of 1,000–1,700 nm (Fig. 1(b)). In particular, the energy transitions involved in Pr^{3+} ion ($^1G_4 \rightarrow {}^3H_5$) and Nd^{3+} ion ($^4F_{3/2} \rightarrow {}^4I_{13/2}$) afford generation of down-conversion luminescence in the NIR-IIa (1,300–1,400 nm) region; and the efficient $^4I_{13/2} \rightarrow {}^4I_{15/2}$ energy transition of Er^{3+} ion provides intense down-conversion emission centered at 1,550 nm in the NIR-IIb (1,500–1,700 nm) region (Fig. 1(b)). In order to populate a resonance level of a RE ion, the lanthanide ion can be excited by directly absorbing the excitation light by itself or receiving excitation energy from another ion or molecule through efficient interionic energy transfer processes, which is the so-called antenna effect (or sensitization) [47].

Taking Er^{3+} as an example, direct excitation of a Er^{3+} ion with 980 nm light can populate the Er^{3+} $^4I_{15/2}$ ground state to its $^4I_{11/2}$ excited level through energy transition of $^4I_{15/2} \rightarrow {}^4I_{11/2}$ with energy bandgap of ~ 10,200 cm^{-1} (ca. 1.29 eV), equal to the energy of a 980 nm photon. Subsequent nonradiative relaxation of Er^{3+} $^4I_{11/2} \rightarrow {}^4I_{13/2}$ leads to a population of $^4I_{13/2}$ state, which is a resonance level for the generation of the 1,550 nm down-conversion NIR-IIb luminescence by radiative transition from $^4I_{13/2}$ to the ground state $^4I_{15/2}$ (Fig. 1(a)). The main NIR-II resonance levels are $^1G_4$ for Pr^{3+} (9,880 cm^{-1}), $^4F_{3/2}$ for Nd^{3+} (11,260 cm^{-1}), $^5I_6$ for Ho^{3+} (8,610 cm^{-1}), $^4I_{13/2}$ for Er^{3+} (6,610 cm^{-1}) and $^3H_4$ for Tm^{3+} (12,720 cm^{-1}). However, several competing processes may occur to reduce the NIR-II down-conversion emission. The first is the upconversion process via multi-photon absorption that excites the RE ion to higher energy levels for subsequent visible or ultraviolet upconversion emission. The second is the luminescence quenching effect caused by nonradiative cross-relaxation process between two neighboring RE ions, or excitation energy transfer/migration to an electron trapping center such as defects or impurity sites. This quenching problem becomes more serious when the RE based NIR-II probes are used for biological application due to the strong energy transfer rate from RE ions to the OH^- groups in aqueous solution (Fig. 1(a)). Therefore, the luminescence efficiency of the RE ion is determined by: (1) the population of the resonance level through either being directly excited or being sensitized; (2) the competing processes including but not limited to upconversion luminescence, nonradiative cross-relaxation and aqueous quenching effect; (3) the intrinsic efficiency of the intra-4f electric-dipole transitions of the RE ions themselves. To date, Er^{3+} and Nd^{3+} have been investigated as the emitter ions in NIR-II probes owing to their luminescence emission in the NIR-II window, centered at 1,550 and 1,050 nm respectively. In the following sections, we will discuss the recent advances in optimizing RE based NIR-II luminescent probes for NIR-II biological imaging.

3 Er^{3+} based NIR-IIb luminescent probes

Fluorescence and luminescence based molecular imaging *in vivo* in the NIR-IIb window (1,500–1,700 nm) afford higher resolution imaging at sub-centimeter tissue depths benefiting from the least light scattering and tissue autofluorescence in the 1,000–1,700 spectral range [23, 48]. However, bright probes in NIR-IIb are scarce. To date, NIR-IIb probes include CNTs [23, 48], inorganic QDs such as lead sulfide (PbS) [49, 50] and indium arsenide [17, 51], and erbium-based rare-earth down-conversion nanoparticles (ErNPs) [18, 52, 53]. Among them, ErNPs have garnered great interest for *in vivo* biological imaging applications owing to their unique properties, including milliseconds long luminescence lifetime, superior photo/chemical stability, and low toxicity. NIR-IIb emission at intense 1,550 nm can be generated through Er^{3+} $^4I_{13/2} \rightarrow {}^4I_{15/2}$ radiative transition (energy difference of ~ 6,500 cm^{-1} or 0.82 eV) for a low Er^{3+} ions doping concentration of ~ 2% (to avoid interionic cross-relaxation) in host materials such as $NaLnF_4$ [54, 55], Ln_2O_3 [56], and LnF_3 [57–59] (Ln = La, Y and Gd). To overcome the weak light absorption problem of the Er^{3+} ion itself due to the low doping concentration, other rare-earth ions such as Yb^{3+} and Nd^{3+} with higher absorption coefficients are co-doped into the host serving as sensitizer to harvest the excitation photons and transfer the excitation energy to Er^{3+}, populating the Er^{3+} $^4I_{13/2}$ state for 1,550 nm luminescence.

3.1 Yb^{3+} ions as sensitizer

Trivalent Yb ion possesses a simple energy-level scheme with only one excited 4f level of $^2F_{5/2}$ [60–65]. The absorption band of Yb^{3+} at around 980 nm due to the $^2F_{7/2} \rightarrow {}^2F_{5/2}$ transition of Yb^{3+} is closely resonant with a large number of f–f transitions in upconverting lanthanide ions (e.g., Er^{3+}, Tm^{3+}, and Ho^{3+}). Note that the Yb^{3+} itself with luminescence in the range of 960–1,040 nm is also an activator candidate for NIR-II probes due to its emission tail > 1,000 nm. The usefulness of the Yb^{3+} ion as a sensitizer for the down-conversion luminescence of ErNPs was first reported by Moghe and his colleagues as early as in 2013 [18]. ErNPs were synthesized as hexagonal-phase core-shell structures consisting of an Yb^{3+} ions and Er^{3+} ions co-doped $NaYF_4$ core surrounded by an undoped $NaYF_4$ shell (Fig. 2(a)). The 1,550 nm emission of this Er^{3+} doped probe occurs following the resonant transfer of excitation energy from Yb^{3+} sensitizer to Er^{3+} activator with an optical efficiency of ~ 1.16% under 980 nm laser excitation. These Er based probes were then encapsulated in human serum albumin to form rare-earth albumin nanocomposites ((RE)ANCs), which demonstrated improved aqueous solubility and biocompatibility (Figs. 2(b) and 2(c)).

In 2015, Paula et al. utilized a layer-by-layer (LbL) assembly method to construct biocompatible ErNPs [53]. In this work, similar RE nanoparticles with 2% Er^{3+} and 20% Yb^{3+} sensitizer were synthesized and followed by LbL modification to endow the nanoparticles with improved biocompatibility and possibility to incorporate therapeutics such as siRNA, inhibitors, or proteins (Fig. 2(d)). Whole-body real-time imaging was carried out by intravenous injection of these LbL-coated NIR-IIb RE probes and excited by a 980 nm laser (Fig. 2(e)). Most organs can be clearly imaged with the accumulation of ErNPs after clearance from the bloodstream. ErNPs with similar structure comprised of Yb^{3+} ion as sensitizer for harvesting 980 nm photons and Er^{3+} ion as activator for 1,550 nm NIR-IIb

emission were also reported by other groups as an offspring of upconversion nanoparticles [66–70].

It is important to produce ErNPs exhibiting bright NIR-IIb luminescence with strong down-conversion in as synthesized form in hydrophobic organic solvents, and equally important to maintain their high brightness when transferred to aqueous phase. For ErNPs NIR-IIb probes, two competing processes exist to their down-conversion luminescence. The first is the upconversion emission process; and the second is quenching of the excited $^4I_{13/2}$ state caused by the OH^- group when ErNPs are transferred to an aqueous solution [35–37]. To overcome these problems, we recently developed an Er-based ErNPs with a 2% Er and 2% Ce doped NaYbF4 core and a NaYF4 shell ($NaYbF_4$:2%Er,2%Ce@$NaYF_4$) with highly boosted down-conversion emission at ~ 1,550 under a 980 nm excitation for NIR-IIb imaging (Figs. 3(a) and 3(b)) [52]. By optimizing the Ce^{3+} ion doping concentration, the lifetime of Er $^4I_{11/2}$ excited state was shortened to increase the population of Er $^4I_{13/2}$ state through accelerated nonradiative relaxation of Er $^4I_{11/2} \rightarrow {}^4I_{13/2}$ facilitated by the Ce^{3+} dopants. An impressive 9-fold enhancement of the down-conversion 1,550 nm luminescence of the ErNPs was achieved, in contrast to the dramatically decreased upconversion emission of the ErNPs at 540 and 650 nm (Fig. 3(c)). In terms of quantum yield (QY), due to discrepancies in the reported QY of the IR-26 reference fluorophore (QYIR26: ~ 0.05%–0.5%), the QY of these ErNPs in aqueous solutions in the NIR-IIb region was estimated to be in the range of 0.27%–2.73% under the 980 nm laser excitation.

For *in vivo* biological imaging, a hydrophilic polymer shell was created on the surface of Ce doped ErNPs by exploiting simple van-der-Waals interactions between the alkyl chains of poly(maleic anhydride-alt-1-octadecene) (PMH) and the oleic acid molecules on the ErNPs. A further PEGylation step was performed through conjugation of methoxy polyethylene glycol amine (mPEG-NH2) onto the nanoparticles to render the ErNPs more biocompatible (Fig. 3(d)). High aqueous dispersion stability and photostability of the PEGylated ErNPs in PBS and fetal bovine serum were confirmed. To reduce the aqueous quenching effect, the thickness of the outer $NaYF_4$ inner layer was optimized to be ~ 7 nm to reach a maximum 1,550 nm emission intensity of the ErNPs in aqueous solution. Although this quenching effect was alleviated to some extent, the 1,550 nm luminescence of the ErNPs was still seriously quenched by 8 times in the water phase relative to in organic phase, and remains a challenge to be further addressed. *In vivo* dynamic mouse brain vessel imaging was performed by exciting the ErNPs with a 980 nm laser while detecting the 1,550 nm luminescence of the intravenously injected PEGylated ErNPs using a much short exposure time of 20 ms (Fig. 3(e)). Due to the low scattering coefficient of the NIR-IIb photons through biological tissue and the nearly zero autofluorescence of tissue in the NIR-IIb range [23, 48], imaging can be done through the intact mouse scalp and skull in a non-invasive manner.

In a recently published paper, Hao and his coworkers prepared a $NaLuF_4$:Gd/Yb/Er/Ce luminescent nanorods with enhanced NIR-IIb emission at 1,525 nm for small tumor/metastasis tumor diagnosis and noninvasive brain/tumor vascular imaging [71]. The down-conversion emission in 1,525 nm was also highly enhanced by boosting the down-conversion pathway and suppressing the upconversion emission via doping of 5% Ce^{3+} ions

(Fig. 3(f)). The QY of these $NaLuF_4$:Gd/Yb/Er/Ce nanorods was measured to be 3.6% in water by using a standard IR-26 dye (QY = 0.5%). These Ce doped RE nanorods were converted to hydrophilic ones before intravenously injected into tumor-bearing mouse. NIR-IIb signal in the tumor site was observed at 24 h post-injection and gradually enhanced until 48 h, revealing the effective accumulation of RE nanorods in the tumor site due to the enhanced permeability and retention (EPR) effect (Fig. 3(g)) [72].

In a more recent work, we demonstrated cubic-phase ErNPs were superior to hexagonal-phase nanoparticles in affording bright NIR-IIb down-conversion luminescence [32]. Specifically, we synthesized a Zn-doped cubic-phase ErNPs with a core-shell structure of $NaYbF_4$:2%Er,2%Ce,10%Zn@$NaYF_4$ (Fig. 4(a)). An ~ 11-fold enhancement of the down-conversion luminescence over the previous brightest hexagonal-phase ErNPs was achieved, through a mechanism of enhancing multi-phonon relaxation in cubic-phase ErNPs over hexagonal-phase, and by reducing crystal field symmetry through Zn^{2+} ion doping. The absolute QY (emission range: 1,300–1,800 nm) of the Zn-doped cubic-phase ErNPs in aqueous solutions was estimated to be ~ 5% using an integrating sphere under the 980 nm laser excitation of 100 mW/cm^2. To impart high stability and biocompatibility to the ErNPs in aqueous and biological media without aggregation and associated toxicity, three hydrophilic cross-linked polymer layers were coated on ErNPs such that the probability of hydrophilic coating detaching from the particles was eliminated (Fig. 4(b)). Owing to the biocompatibility derived from the reliable cross-linked polymer network on the surface of ErNPs and their small hydrated size of ~ 35.5 nm, a rapid biliary excretion of the intravenously injected ErNPs was observed (Fig. 4(c)), which could facilitate potential future clinical translation of the nanoparticles.

Importantly, the outmost layer of the ErNPs containing eight-arm branched polyethylene glycol amine (8Arm-PEG-NH_2) layer imparts amine groups to allow conjugation of anti-PD-L1 antibody to the ErNPs (ErNPs-aPDL1). *In vivo* NIR-IIb molecular imaging of PD-L1 was done after intravenous injection of ErNPs-aPDL1 into the tail vein of BALB/c mice bearing PD-L1 over-expressed CT-26 tumor (Fig. 4(d)). The high brightness of ErNPs-aPLD1 combined with low autofluorescence background in NIR-IIb range and high affinity of the conjugated anti-PD-L1 antibody towards PD-L1 ligands are crucial to afford molecular PD-L1 imaging of biological targets in tumor with unprecedented tumor to normal tissue (T/NT) ratio > 40 (Fig. 4(e)), remarkably higher than previous fluorescence-based molecular tumor imaging (Figs. 4(f) and 4(g)) using fluorophores emitting in shorter wavelength ranges (T/NT ratios are typically ~ 2–4 in the 700–900 nm NIR-I range, and ~ 8–12 in the ~ 1,100 nm NIR-II range).

Encouraged by the above robust ErNPs-aPLD1 molecular PD-L1 targeting agent and the long-lived NIR-IIb luminescence (~ 4.3 ms in aqueous solution) of the ErNPs, a time-resolved imaging technique (Figs. 5(a) and 5(b)) was developed to differentiate ErNPs luminescence from short-lived NIR-IIb fluorescence (~ 46 μs) of PbS QDs (Fig. 5(c)) for two-plex molecular imaging in the same 1,500–1,700 nm NIR-IIb emission range. To target the $CD8^+$ cytotoxic T lymphocytes (CTLs) *in vivo*, the PbS QDs were conjugated with anti-CD8α antibody (PbS-aCD8) for tracking the $CD8^+$ cells in response to PD-L1 checkpoint blockade cancer immunotherapy. Two-plex NIR-IIb molecular imaging strategy combing ~

1,600 nm emitting ErNPs-aPDL1 and PbS-aCD8 can simultaneously mapping out the heterogeneous bio-distribution of PD-L1 and $CD8^+$ CTLs within the tumor microenvironment and in main organs (Figs. 5(d) and 5(e)). When zooming in to the tumor, we imaged noninvasively through the skin to glean ErNPs-aPDL1 NIR-IIb signals circulating in the tortuous tumor vasculature at 5 min p.i., resolving vessels in CT-26 tumor down to micrometer spatial resolution. Leakage of ErNPs-aPDL1 from blood vessels into tumor tissue was also observed (Fig. 5(d)), indicating the start of ErNPs-aPDL1 extravasation and binding to cancer cells within the tumor. At 24 h post-injection of ErNPs-aPDL1 and PbS-aCD8, the shape of the CT-26 tumor was clearly visualized in the ErNPs channel with a relatively even signal distribution through the tumor (Fig. 5(e)). However, for the PbS-aCD8 channel, the signals were higher around the periphery of the tumor and extending inward (Fig. 5(e)). This suggested the infiltration of immune-competent $CD8^+$ CTLs starting primarily from the periphery region of the CT-26 tumor, which was limited by vascular hyper-permeability and shortage of functional lymphatic vessels inside solid tumors.

In particular, *in vivo* evaluation of the distribution and proportion of $CD8^+$ CTLs in tumor vs. spleen (a lymphoid organ) was also performed to assess the activation status of T cells (Fig. 5(f)). By plotting of $CD8^+$ T cells signal ratio between tumor and spleen (T/spleen), the (T/spleen)_CD8 ratio of ~ 5.3 was measured in immune activated CT-26 tumor mice (received PD-L1 immunotherapy), which was > 15 times higher than immune non-activated tumor mice. This result suggested that noninvasive *in vivo* two-plex NIR-IIb imaging to glean tumor PD-L1 level and CD8+ T cell distribution in tumor vs. spleen could provide useful parameters for assessing response to immunotherapy and complement *ex vivo* biopsy-based diagnostic methods.

3.2 Nd^{3+} ions as sensitizer

The intense absorption cross-section of Nd^{3+} at around 740 nm ($^4I_{9/2} \rightarrow {}^4F_{7/2}$), 800 nm ($^4I_{9/2} \rightarrow {}^4F_{5/2}$) and 850 nm ($^4I_{9/2} \rightarrow {}^4F_{3/2}$), and efficient energy transfer from excited Nd^{3+} to Yb^{3+} via interionic cross-relaxation [$(^4F_{3/2})_{Nd}$, $(^2F_{7/2})_{Yb}$] → [$(^4I_{9/2})_{Nd}$, $(F_{5/2})_{Yb}$], making Nd^{3+} ion a promising sensitizer for the down-conversion luminescence of Er^{3+} ion [73, 74]. In 2014, Zhang et al. reported a novel kind of multi-shell hexagonal-phase RE nanocrystals containing 4 layers with a structure of $NaGdF_4$/Na(Gd,Yb)F_4:Er/$NaYF_4$:Yb/$NaNdF_4$:Yb (Fig. 6(a)) [75]. In this nanocrystal, the Nd^{3+} ion in the outmost $NaNdF_4$:Yb shell acts as the sensitizer by absorbing the 800 nm excitation light. The excitation energy of the excited Nd^{3+} is then transferred to Yb^{3+} and migrating within these layers by the co-doped Yb^{3+} ions until the Er^{3+} in the inner shell is sensitized. This results in relaxation from the excited state of Er^{3+} through the emission of a 1,525 nm photon ($^4I_{13/2} \rightarrow {}^4I_{15/2}$). The excitation at 800 nm is located in the biological transparency window with lower absorption by water and heat generation than at 980 nm, and is a more desirable excitation wavelength than 980 nm with the least perturbance to biological tissues [76]. These 800 nm sensitized RE nanocrystals were transferred from the organic phase to the aqueous phase by coating amphiphilic 1,2-distearoyl-sn-glycero-3-phosphoethanolamine-N-[carboxy-(polyethylene glycol)-2000] (DSPE-PEG2000-COOH) phospholipids onto their surface to form nanocrystal-phospholipid micelle complexes. *In vivo* bio-imaging experiments were also

carried out by delivering these hydrophilic RE nanocrystals to the mouse stomach using a gastric syringe. Upon 800 nm laser irradiation, bright 1,525 nm luminescence signals were detected in the mouse stomach which is determined to be 0.8–1.2 cm depth in the mouse body.

In a typical Nd^{3+} sensitized core-shell-shell structured RE nanocrystal, the energy transfer from the Nd^{3+} sensitizer to the Er^{3+} activator is bridged by these layers containing Yb^{3+} ions dopants through energy migration over the Yb^{3+} sublattice; and the thickness of these layers plays a key role in the efficiency and performance of this interionic energy transfer/migration (Fig. 6(b)) [77]. In a recently published paper, Zhang et al. designed a series of lifetime-engineered Er^{3+} doped RE nanoparticles for multiplexed NIR-IIb *in vivo* imaging [77]. Employing Nd^{3+} sensitizers and Er^{3+} emitters, these nanoparticles absorb 808 nm excitation and emit luminescence centered at 1,525nm. The nanoparticle consists of an outer layer co-doped with Nd^{3+} and Yb^{3+}, an intermediate layer doped with Yb^{3+} only, and an inner layer co-doped with Yb^{3+} and Er^{3+} (Fig. 6(b)). This core-shell-shell structure allows the luminescence lifetime tuning systematically in two directions: (1) increasing the thickness of the energy relay layer prolongs the average process from absorption to emission, leading to a longer lifetime (Fig. 6(c)); (2) at a given thickness of the energy relay layer corresponding to identical capacity of the Yb^{3+} sublattice, an increase in the Er^{3+} concentration accelerates the conversion of stored energy into luminescence emission, which shortens the lifetime (Fig. 6(d)). By tuning the intermediate layer thickness and Er^{3+} doping concentration, a substantial lifetime-selectable range spanning three orders of magnitude was demonstrated for the Er^{3+} 1,525 nm emission, easily accommodating more than 10 distinct lifetime identities that were clearly distinguished using a time-resolved imaging system (Fig. 6(e)).

With this NIR-IIb luminescence lifetime-resolved multiplexing imaging approach, the researcher further explored its potential for cancer diagnostics *in vivo* (Fig. 6(f)). Three lifetime populations of the Er nanoparticles were conjugated with primary antibodies against three routinely examined biomarkers for breast cancer: estrogen receptor (ER), progesterone receptor (PR) and human epidermal growth factor receptor-2 (HER2). The NIR-IIb luminescence from the tumors was sufficiently high to distinguish the positive groups from the control group. This allowed quantification of the biomarker expressions of the tumor subtype by resolving the three lifetime components simultaneously using a pattern recognition algorithm, which was consistent with the *in vitro* western blot results, demonstrating the potential of this *in vivo* multiplexing imaging method for *in vivo* image and point-of-care diagnostics.

3.3 Er^{3+} ions as sensitizer

Although there are several intense absorption lines of Er^{3+} at around 650 nm ($^4I_{15/2} \rightarrow {}^4F_{9/2}$), 808 nm ($^4I_{15/2} \rightarrow {}^4I_{9/2}$), and 980 nm ($^4I_{15/2} \rightarrow {}^4I_{11/2}$), one critical limitation of Er^{3+} doped NIR-IIb luminescence nanocrystals is the weak absorbance of Er^{3+} ions due to the relatively low Er^{3+} emitter doping concentration (typically 1 mol%–5 mol%). The luminescence intensity decreases sharply with increasing the doping ratio, commonly referred to as “concentration quenching”. There are two common explanations for the

concentration quenching problem: (1) increased interionic nonradiative cross-relaxation processes; (2) enhanced energy migration via resonant energy transfer to the surface defects [78, 79]. Recently, Almutairi et al. demonstrated that the major quenching process at high dopant concentrations is predominantly due to energy migration to the surface and not cross-relaxation between dopant ions [80]. Based on this, a new class of Er^{3+} based NIR-IIb probe was synthesized with a structure of $NaErF_4@NaLuF_4$ (Fig. 7(a)). In the inner NaErF4 core, the Er^{3+} ion acts as both activator and sensitizer by absorbing the 980 nm excitation photons to populate its $^4I_{11/2}$ state. Nonradiative relaxation of Er $^4I_{11/2} \rightarrow {}^4I_{13/2}$ occurs subsequently, followed by generating of intense NIR-IIb luminescence centered at 1,550 nm via radiative relaxation from the Er^{3+} $^4I_{13/2}$ excited state to the $^4I_{15/2}$ ground state (Fig. 7(b)). The inert NaLuF4 with an optimal thickness of ~ 8 nm is essential to suppress the excitation energy migration to the surface quenching defects. In this case, no “concentration quenching” is observed in the lifetime or the emission of this core-shell nanocrystal. By tuning the Er^{3+} doping concentration from 5% to 100% in $NaYF_4$:n%Er@$NaLuF_4$ nanocrystal, the 100% Er^{3+} doping ratio is found to be the brightest one under both 658 and 808 nm excitation (Figs. 7(c) and 7(d)).

Recent works also show that the co-doping of other rare-earth or transition metal ions can further improve the luminescence intensity of this Er^{3+}-sensitized RE nanocrystal [81, 82]. For example, Chen and coworkers reported a class of Er^{3+}-sensitized and enriched core-shell nanocrystals ($NaErF_4$:Yb@$NaLuF_4$) with enhanced 1,525 nm luminescence under 808 nm excitation [82]. The highly doped Er^{3+} ions (80%) impart strong absorption coefficient at 808 nm to the nanocrystal, enabled self-sensitization process of Er^{3+} to generate intense 1,525 nm NIR-IIb luminescence. Importantly, an approximately 2-fold enhancement of the NIR-IIb emission is achieved by doping of 20% Yb^{3+} ions into the core layer to form $NaErF_4$:20%Yb@$NaLuF_4$ (Fig. 7(e)). The researchers suggested that the doped Yb^{3+} ions act as energy trapping center for the Er^{3+} ions by efficient interionic cross-relaxation between Er^{3+} $^4I_{11/2}$ state and Yb^{3+} $^2F_{5/2}$ state (Fig. 7(f)). This energy trapping effect can suppress the process of excitation energy migration to lattice defects inside the $NaErF_4$:Yb core layer, and induce energy back transfer process to populate the Er^{3+} $^4I_{13/2}$ level, thus become favorable for the NIR-IIb luminescence of RE nanocrystal. The QY of these $NaErF_4$:Yb@$NaLuF_4$ nanocrystals was determined to be ~ 11% (emission range: 900–1,700 nm) under 808 nm excitation using ICG dye (QY = 12%) as a reference standard. The researchers then performed a ligand exchange procedure to coat the $NaErF_4$:Yb@$NaLuF_4$ nanocrystal with polyacrylic acid (PAA) hydrophilic polymer, rendering the RE nanocrystal dispersible in aqueous solution. After injection of this hydrophilic NIR-IIb probe, a clear high resolution and high contrast NIR-IIb luminescence image of mouse brain vessel (Fig. 7(g)) can be obtained under 808 nm laser excitation with a short exposure time of 10 ms, demonstrating the advantages of this Er^{3+}-sensitized RE nanocrystal for optical imaging with reduced light scattering and autofluorescence in the NIR-IIb range.

4 Nd^{3+} based NIR-II luminescent probes

In the past few decades, the Nd^{3+} doped garnet crystals have been pursued as the most promising laser materials to achieve 1.3 and 1.06 μm NIR lasing [83, 84]. The radiative energy transitions of $^4F_{3/2} \rightarrow {}^4I_{11/2}$ and $^4F_{3/2} \rightarrow {}^4I_{13/2}$ in Nd^{3+} ion enable the generation of

intense NIR-II luminescence peaked at 1,050 and 1,330 nm, respectively [85, 86]. Nd^{3+} based NIR-II luminescent probes have been under development for optical bio-imaging in recent years. The doping of Nd^{3+} ion has been attempted in a variety of nanosized host materials including CaF_2 [87], SrF_2 [88], LaF_3 [89], $LiLnF_4$ [90, 91] and $NaLnF_4$ [85, 92–96] (Ln = Y, Gd and Lu), in which the Nd^{3+} dopant acts as both activator and sensitizer. In contrast to the Er^{3+}, the doping of Nd^{3+} suffers from a severe concentration quenching problem even being embedded in the core layer of a core-shell structured nanocrystal; thus the reported optimal Nd^{3+} doping concentration is about 1 mol%–5 mol%. Nevertheless, the relatively high absorption coefficient of Nd^{3+} at 730 and 800 nm, and the efficient Nd^{3+} $^4F_{3/2} \rightarrow {}^4I_{11/2}$ (1,050 nm) and $^4F_{3/2} \rightarrow {}^4I_{13/2}$ (1,330 nm) radiative transitions have made the Nd^{3+} based RE phosphor a useful NIR-II probe emitting in the 1,000–1,350 nm spectral range.

In 2017, Zhang et al. reported a Nd^{3+} based NIR-II fluorescent mesoporous microcarrier with Nd^{3+} based nanocrystals (NdNCs) embedding in the framework of a SiO_2 particle coated with a mesoporous SiO_2 shell ($mSiO_2$-Nd) (Fig. 8(a)) [97]. By combining the multi-excitation properties of the Nd^{3+} based nanocrystal (can be excited by both 730 and 808 nm light) and a NPTAT-protein complex (NPTAT is an organic phthalocyanine dye with a maximum absorption at 625 nm) loaded into the mesopores of the $mSiO_2$-Nd, a protein-release monitoring probe was prepared. The high absorption coefficient of the NPTAT at 730 nm can dramatically quench the 1,060 nm luminescence of NdNCs when excited by 730 nm light. Whilst under 808 nm excitation, the NdNCs 1,060 nm emission was barely influenced by the NPTAT due to the weak absorbance of NPTAT at 808 nm (Fig. 8(b)). Thus the drug-release process can be monitored and quantified based on these interesting characteristics with NIR-II bio-imaging under 730 nm excitation while tracking the fate of the $mSiO_2$-Nd microcarriers under 808 nm excitation. *In vivo* NIR-II bio-imaging experiments (Fig. 8(c)) clearly demonstrated that the intensity of the 1,060 nm luminescence excited by the 808 nm laser was related to the quantity of the $mSiO_2$-Nd in real time, while the intensity of the signals excited by the 730 nm laser reflected the drug-release percentage (Figs. 8(d) and 8(e)). Such NIR-II bio-imaging technique can complement the traditional radio-isotope tracing method to realize non-invasive *in vivo* drug-release monitoring.

Apart from the inorganic nanocrystals doped with lanthanide ions, organic molecule-based RE ion complexes exhibiting NIR-II luminescence are also particularly interesting because of their small sizes [98, 99]. The stable binding of a RE ion in a water-soluble macromolecule requires a very strong binding chelator to compete against water molecules which can strongly bind to the RE ion themselves [100]. In a recent work, Hao and his coworkers prepared a NIR-II molecular Nd-based complex (Nd-DTPA) through chelation of Nd^{3+} with diethylene triamine pentaacetate acid (DTPA), which offers four carboxylic acid groups for binding the Nd^{3+} ion (Fig. 9(a)) [101]. Efficient narrow band NIR-II emission centered at 1,050 and 1,330 nm are obtained by exciting the Nd-DTPA with an 808 nm laser (Fig. 9(b)). By using a standard IR-26 dye (dissolved in dichloroethanes; the quantum yield of IR-26 dye is deemed to be 0.5%) as a reference, the quantum yield of Nd-DTPA at 1,050 nm is measured to be 0.63%, making it a useful NIR-II probe for *in vivo* bio-imaging. The Nd-DTPA exhibited high biocompatibility and could be directly intravenously injected to the mice without any further hydrophilic treatment. Within a few seconds post-injection, strong

luminescence signal can be observed in kidney due to the fast accumulation of Nd-DTPA for renal excretion (Fig. 9(c)). Unlike nanoparticle probes, retention of the Nd-DTPA in the liver and spleen is much lower without obvious NIR-II signal detected in these two organs. A strong signal of Nd-DTPA can be observed in bladder within 10 min post-injection, demonstrating the rapid excretion of the Nd-DTPA complex from the kidney to the bladder through the renal system. Indeed, the Nd-DTPA probe can be fully excreted from the mice within 11 h, confirming fast renal clearance of the Nd-DTPA molecule. These findings will open up the possibility for designing RE complex with high biocompatibility, fast excretion speed, low toxicity and strong NIR-II luminescence for *in vivo* optical imaging and potential clinic translation.

5 Current status and future directions

The impressive *in vivo* imaging quality and clarity by detecting long-wavelength emitted light in the NIR-II window have stimulated tremendous research interest and activities in this area in recent years [102]. We anticipate a bright future of NIR-II bio-imaging towards obtaining understanding of biology with unprecedented spatial and temporal resolutions in living mammals at millimeters tissue depth. Future development and applicability of *in vivo* NIR-II fluorescence/luminescence bio-imaging will continue to hinge on the optical properties of the probes, and rare-earth nanoparticles are undoubtedly an excellent class of NIR-II emitters.

Rare earth-based materials have already afforded fascinating luminescence applications with great performances in diverse areas of modern optic/optoelectronic technologies and devices, such as semiconductor lasers, solar systems and television & computer screens. Their rich optical properties include upconversion and down-conversion luminescence spanning a broad spectral range from 300 to 3,000 nm, and have generated great scientific and practical interest. While upconversion nanocrystals have been investigated for decades, the exploitation of the NIR-II down-conversion luminescent RE compounds as bio-probes for the *in vivo* bio-imaging techniques was commenced only recently, motivated by the rapid progresses in the field of biotechnology and nanotechnology. In this review we have provided an overview of various recent work on RE-based NIR-II probes in small animal *in vivo* bio-imaging. It is important to point out that the ~ 1,500–1,700 nm NIR-IIb window is the most beneficial spectral range in the 1,000–1,700 nm NIR-II window due to minimal light scattering and lowest autofluorescence. Hence, even though common probes such as ICG and IRDye800 with emission tail > 1,000 nm can be utilized for NIR-II imaging in the 1,000–1,300 nm range, rare earth nanoparticles emission in NIR-IIb are superior to ICG and other organic fluorophores in terms of imaging clarity and signal/background ratios. Molecular imaging with existing organic dyes in the NIR-IIa window is also inferior to NIR-IIb with ErNPs, as found in the *in vivo* PD-L1 imaging work (Fig. 3(f) vs. Fig. 3(d)). The Er based nanoparticle NIR-IIb probes are also unmatched by quantum dots in composition due to the non-toxic elements. These considerations make ErNPs the most ideal NIR-II probe developed thus far. The layer-by-layer crosslinked surface coating can enable rapid fecal excretion of ErNPs, making them useful for potential human use without long-term toxicity concerns.

Although exciting advancements have been made in developing and utilizing the NIR-II lanthanide luminescence for a variety of bio-imaging/analysis techniques, challenges still remained for RE-based NIR-II probes. Firstly, the emission intensity of the RE probes is still not fully optimized and can be further boosted. Despite their unique optical properties including narrow-band emission and superior photostability, the engineering of RE probes for higher emission efficiency is a long-standing challenge to researchers. A strong and stable emission of RE probes could facilitate the dynamically monitoring of physiological processes by decreasing the applied camera exposure time, and allow microscopy imaging by providing sufficient emission intensity in the desired focal point. To date, Er^{3+} and Nd^{3+} have been utilized for the design of NIR-II probes, while other candidate lanthanide ions including Pr^{3+}, Ho^{3+}, and Tm^{3+} are rarely reported for the application of NIR-II bio-imaging mainly due to their low luminescence efficiency. In the case of Er^{3+} and Nd^{3+}, the harsh quenching problem caused by the hydroxyl groups in aqueous solution has been a latent and severe limitation to their luminescence intensity in biological environment. Their NIR-II emission could be further degraded by the numerous competing processes such as upconversion luminescence, nonradiative cross-relaxation, and excitation energy losses through migration to the crystal defects. All of these aspects should be carefully investigated and improved to promote the development of ultra-bright RE NIR-II probes.

Secondly, the biocompatibility and biostability of RE NIR-II probes need to be further investigated and improved. The superior biocompatibility of the exogenously introduced RE probes is essential to guarantee their nonbiological toxicity and rapid excretion from body. When conjugated with targeting moieties such as antibody, peptide and diabody, the biocompatibility of RE-moieties agents should be outstanding to ensure the correlation between the signal intensities of the RE probes and the expression levels of the biomarkers. Almost all of the currently developed RE NIR-II probes are lanthanide-based nanocrystals, which cannot be utilized directly for biological systems without surface modification. Tremendous efforts have been expended to improve the surface modification methods for RE-base nanoparticles ever since the developing and applying of the upconversion nanoparticles, but the outcome is limited and far from satisfactory for clinical translation. Experimentally, we observed that hydrophilic treatments of RE nanoparticles are more challenging than for inorganic QDs, possible due to the weaker interaction between surface ligands and lanthanide ions, which causes the detaching of the hydrophilic coating from the particles and consequent aggregation. In view of this, our recently developed hydrophilic cross-linked coating layers could be a promising approach to impart the RE nanoparticles with superior biocompatibility by forming a capping network to prevent exfoliation of the surface polymeric coating. Nevertheless, there is still a long way to go to show that the highly biocompatible RE nano-probes in mice are safe to use for humans in the clinic.

Thirdly, the unique optical characteristics of RE NIR-II probes remain to be fully investigated and exploited. One outstanding feature of lanthanide luminescence is the long and tunable lifetime, useful for near zero-background imaging and multiplexed probing of several biological targets in the same beneficial NIR-II window. Another attractive feature of luminescent RE compounds is their narrow-band emission, resulting in a high color purity of the emitted NIR-II light, potential for the multi-color NIR-II bio-imaging. These multiplexed and multi-color NIR-II bio-imaging probes will enable simultaneous imaging of multiple

molecular and biological targets at single cell level inside a living body, allowing molecular imaging at unprecedented multiplexity, spatial/temporal resolution and depth.

Finally, the RE-based NIR-II probes are of high biocompatibility and low toxicity, making them promising for a variety of medical diagnosis application and potential clinical translation. To this end, we believe the future development trend of NIR-II bio-imaging technology using RE-based luminescent probes are as follows: (1) ultrafast dynamic *in vivo* imaging with sub-microsecond temporal resolution to reveal the physiological and pathological process in the body; (2) non-invasive or minimally-invasive NIR-II microscope optical imaging with three-dimensional reconstruction techniques such as confocal or light-sheet microscopy to mapping out the micron-scale biological structures down to cellular level; (3) molecular imaging with binding moieties such as small molecule drugs, tumor/immune system targeted antibodies, genome engineering related RNA, DNA and proteins to provide evolutionary pathological research methods and tumor detection techniques.

Acknowledgements

This work was supported by the National Institutes of Health (grant no. DP1-NS-105737).

References

[1]. Hong GS; Antaris AL; Dai HJ Near-infrared fluorophores for biomedical imaging. Nat. Biomed. Eng 2017, 1, 0010.

[2]. Rao JH; Dragulescu-Andrasi A; Yao HQ Fluorescence imaging *in vivo*: Recent advances. Curr. Opin. Biotechnol 2007, 18, 17–25. [PubMed: 17234399]

[3]. Hong GS; Lee JC; Robinson JT; Raaz U; Xie LM; Huang NF; Cooke JP; Dai HJ Multifunctional *in vivo* vascular imaging using near-infrared II fluorescence. Nat. Med 2012, 18, 1841–1846. [PubMed: 23160236]

[4]. Welsher K; Liu Z; Sherlock SP; Robinson JT; Chen Z; Daranciang D; Dai HJ A route to brightly fluorescent carbon nanotubes for near-infrared imaging in mice. Nat. Nanotechnol 2009, 4, 773–780. [PubMed: 19893526]

[5]. Antaris AL; Chen H; Cheng K; Sun Y; Hong GS; Qu CR; Diao S; Deng ZX; Hu XM; Zhang B et al. A small-molecule dye for NIR-II imaging. Nat. Mater 2016, 15, 235–242. [PubMed: 26595119]

[6]. Yang QL; Ma ZR; Wang HS; Zhou B; Zhu SJ; Zhong YT; Wang JY; Wan H; Antaris A; Ma R et al. Rational design of molecular fluorophores for biological imaging in the NIR-II window. Adv. Mater 2017, 29, 1605497.

[7]. Li BH; Lu LF; Zhao MY; Lei ZH; Zhang F An efficient 1,064 nm NIR-II excitation fluorescent molecular dye for deep-tissue high-resolution dynamic bioimaging. Angew. Chem., Int. Ed 2018, 57, 7483–7487.

[8]. Sun Y; Ding MM; Zeng XD; Xiao YL; Wu HP; Zhou H; Ding BB; Qu CR; Hou W; Er-bu AGA et al. Novel bright-emission small-molecule NIR-II fluorophores for *in vivo* tumor imaging and image-guided surgery. Chem. Sci 2017, 8, 3489–3493. [PubMed: 28507722]

[9]. Zhu SJ; Yang QL; Antaris AL; Yue JY; Ma ZR; Wang HS; Huang W; Wan H; Wang J; Diao S et al. Molecular imaging of biological systems with a clickable dye in the broad 800- to 1,700-nm near-infrared window. Proc. Natl Acad. Sci. USA 2017, 114, 962–967. [PubMed: 28096386]

[10]. Hong GS; Diao S; Chang JL; Antaris AL; Chen CX; Zhang B; Zhao S; Atochin DN; Huang PL; Andreasson KI et al. Through-skull fluorescence imaging of the brain in a new near-infrared window. Nat. Photonics 2014, 8, 723–730. [PubMed: 27642366]

[11]. Gong H; Peng R; Liu Z Carbon nanotubes for biomedical imaging: The recent advances. Adv. Drug Del. Rev 2013, 65, 1951–1963.

[12]. Diao S; Hong GS; Robinson JT; Jiao LY; Antaris AL; Wu JZ; Choi CL; Dai HJ Chirality enriched (12,1) and (11,3) single-walled carbon nanotubes for biological imaging. J. Am. Chem. Soc 2012, 134, 16971–16974. [PubMed: 23033937]

[13]. Robinson JT; Hong GS; Liang YY; Zhang B; Yaghi OK; Dai HJ *In vivo* fluorescence imaging in the second near-infrared window with long circulating carbon nanotubes capable of ultrahigh tumor uptake. J. Am. Chem. Soc 2012, 134, 10664–10669. [PubMed: 22667448]

[14]. Bardhan NM; Ghosh D; Belcher AM Carbon nanotubes as *in vivo* bacterial probes. Nat. Commun 2014, 5, 4918. [PubMed: 25230005]

[15]. Wan H; Yue JY; Zhu SJ; Uno T; Zhang XD; Yang QL; Yu K; Hong GS; Wang JY; Li LL et al. A bright organic NIR-II nanofluorophore for three-dimensional imaging into biological tissues. Nat. Commun 2018, 9, 1171. [PubMed: 29563581]

[16]. Tao ZM; Hong GS; Shinji C; Chen CX; Diao S; Antaris AL; Zhang B; Zou YP; Dai HJ Biological imaging using nanoparticles of small organic molecules with fluorescence emission at wavelengths longer than 1000 nm. Angew. Chem., Int. Ed 2013, 52, 13002–13006.

[17]. Bruns OT; Bischof TS; Harris DK; Franke D; Shi YX; Riedemann L; Bartelt A; Jaworski FB; Carr JA; Rowlands CJ et al. Next-generation *in vivo* optical imaging with short-wave infrared quantum dots. Nat. Biomed. Eng 2017, 1, 0056. [PubMed: 29119058]

[18]. Naczynski DJ; Tan MC; Zevon M; Wall B; Kohl J; Kulesa A; Chen S; Roth CM; Riman RE; Moghe PV Rare-earth-doped biological composites as *in vivo* shortwave infrared reporters. Nat. Commun 2013, 4, 2199. [PubMed: 23873342]

[19]. Zhang Y; Hong GS; Zhang YJ; Chen GC; Li F; Dai HJ; Wang QB Ag_2S quantum dot: A bright and biocompatible fluorescent nanoprobe in the second near-infrared window. ACS Nano 2012, 6, 3695–3702. [PubMed: 22515909]

[20]. Liang L; Chen N; Jia YY; Ma QQ; Wang J; Yuan Q; Tan WH Recent progress in engineering near-infrared persistent luminescence nanoprobes for time-resolved biosensing/bioimaging. Nano Res. 2019, 12, 1279–1292.

[21]. Hu F; Li CY; Zhang YJ; Wang M; Wu DM; Wang QB Real-time *in vivo* visualization of tumor therapy by a near-infrared-II Ag_2S quantum dot-based theranostic nanoplatform. Nano Res. 2015, 8, 1637–1647.

[22]. Ortgies DH; García-Villalón ÁL; Granado M; Amor S; Rodríguez EM; Santos HDA; Yao JK; Rubio-Retama J; Jaque D Infrared fluorescence imaging of infarcted hearts with Ag_2S nanodots. Nano Res. 2019, 12, 749–757.

[23]. Diao S; Blackburn JL; Hong GS; Antaris AL; Chang JL; Wu JZ; Zhang B; Cheng K; Kuo CJ; Dai HJ Fluorescence imaging *in vivo* at wavelengths beyond 1,500 nm. Angew. Chem., Int. Ed 2015, 54, 14758–14762.

[24]. Huang S; Peng S; Li YB; Cui JB; Chen HL; Wang LY Development of NIR-II fluorescence image-guided and pH-responsive nanocapsules for cocktail drug delivery. Nano Res. 2015, 8, 1932–1943.

[25]. Wang ZM; Upputuri PK; Zhen X; Zhang RC; Jiang YY; Ai XZ; Zhang ZJ; Hu M; Meng ZY; Lu YP et al. pH-sensitive and biodegradable charge-transfer nanocomplex for second near-infrared photoacoustic tumor imaging. Nano Res. 2019, 12, 49–55.

[26]. Wan H; Ma HL; Zhu SJ; Wang FF; Tian Y; Ma R; Yang QL; Hu ZB; Zhu T; Wang WZ et al. Developing a bright NIR-II fluorophore with fast renal excretion and its application in molecular imaging of immune checkpoint PD-L1. Adv. Funct. Mater 2018, 28, 1804956. [PubMed: 31832053]

[27]. Kamimura M; Matsumoto T; Suyari S; Umezawa M; Soga K Ratiometric near-infrared fluorescence nanothermometry in the OTN-NIR (NIR II/III) biological window based on rare-earth doped β-$NaYF_4$ nanoparticles. J. Mater. Chem. B 2017, 5, 1917–1925. [PubMed: 32263945]

[28]. Zhu SJ; Herraiz S; Yue JY; Zhang MX; Wan H; Yang QL; Ma ZR; Wang Y; He JH; Antaris AL et al. 3D NIR-II molecular imaging distinguishes targeted organs with high-performance NIR-II bioconjugates. Adv. Mater 2018, 30, 1705799.

[29]. Tao ZM; Dang XN; Huang X; Muzumdar MD; Xu ES; Bardhan NM; Song HQ; Qi RG; Yu YJ; Li T et al. Early tumor detection afforded by *in vivo* imaging of near-infrared II fluorescence. Biomaterials 2017, 134, 202–215. [PubMed: 28482280]

[30]. Wang FF; Wan H; Ma ZR; Zhong YT; Sun QC; Tian Y; Qu LQ; Du H; Zhang MX; Li LL et al. Light-sheet microscopy in the near-infrared II window. Nat. Methods 2019, 16, 545–552. [PubMed: 31086342]

[31]. Liu CY; Hou Y; Gao MY Are rare-earth nanoparticles suitable for *in vivo* applications? Adv. Mater 2014, 26, 6922–6932. [PubMed: 24616057]

[32]. Zhong YT; Ma ZR; Wang FF; Wang X; Yang YJ; Liu YL; Zhao X; Li JC; Du HT; Zhang MX et al. *In vivo* molecular imaging for immunotherapy using ultra-bright near-infrared-IIb rare-earth nanoparticles. Nat. Biotechnol 2019, 37, 1322–1331. [PubMed: 31570897]

[33]. Hoshyar N; Gray S; Han HB; Bao G The effect of nanoparticle size on *in vivo* pharmacokinetics and cellular interaction. Nanomedicine 2016, 11, 673–692. [PubMed: 27003448]

[34]. Clough TJ; Jiang LJ; Wong KL; Long NJ Ligand design strategies to increase stability of gadolinium-based magnetic resonance imaging contrast agents. Nat. Commun 2019, 10, 1420. [PubMed: 30926784]

[35]. Gapontsev VP; Matitsin SM; Isineev AA; Kravchenko VB Erbium glass lasers and their applications. Opt. Laser Technol 1982, 14, 189–196.

[36]. Yan YC; Faber AJ; de Waal H Luminescence quenching by OH groups in highly Er-doped phosphate glasses. J. Non-Cryst. Solids 1995, 181, 283–290.

[37]. Zhang L; Hu HF The effect of OH^- on IR emission of Nd^{3+}, Yb^{3+} and Er^{3+} doped tetraphosphate glasses. J. Phys. Chem. Solids 2002, 63, 575–579.

[38]. Binnemans K Lanthanide-based luminescent hybrid materials. Chem. Rev 2009, 109, 4283–4374. [PubMed: 19650663]

[39]. Eliseeva SV; Bünzli JCG Lanthanide luminescence for functional materials and bio-sciences. Chem. Soc. Rev 2010, 39, 189–227. [PubMed: 20023849]

[40]. Wang F; Liu XG Recent advances in the chemistry of lanthanide-doped upconversion nanocrystals. Chem. Soc. Rev 2009, 38, 976–989. [PubMed: 19421576]

[41]. Boyn R 4f–4f luminescence of rare-earth centers in II–VI compounds. Phys. Status Solidi B 1988, 148, 11–47.

[42]. Weber MJ Radiative and multiphonon relaxation of rare-earth ions in Y_2O_3. Phys. Rev 1968, 171, 283–291.

[43]. Saisudha MB; Ramakrishna J Effect of host glass on the optical absorption properties of Nd^{3+}, Sm^{3+}, and Dy^{3+} in lead borate glasses. Phys. Rev. B 1996, 53, 6186–6196.

[44]. Chen GY; Liu HC; Liang HJ; Somesfalean G; Zhang ZG Upconversion emission enhancement in Yb^{3+}/Er^{3+}-codoped Y_2O_3 nanocrystals by tridoping with Li^+ ions. J. Phys. Chem. C 2008, 112, 12030–12036.

[45]. Ofelt GS Intensities of crystal spectra of rare-earth ions. J. Chem. Phys 1962, 37, 511–520.

[46]. Judd BR Optical absorption intensities of rare-earth ions. Phys. Rev 1962, 127, 750–761.

[47]. Zou WQ; Visser C; Maduro JA; Pshenichnikov MS; Hummelen JC Broadband dye-sensitized upconversion of near-infrared light. Nat. Photonics 2012, 6, 560–564.

[48]. Diao S; Hong GS; Antaris AL; Blackburn JL; Cheng K; Cheng Z; Dai HJ Biological imaging without autofluorescence in the second near-infrared region. Nano Res. 2015, 8, 3027–3034.

[49]. McDonald SA; Konstantatos G; Zhang SG; Cyr PW; Klem EJD; Levina L; Sargent EH Solution-processed PbS quantum dot infrared photodetectors and photovoltaics. Nat. Mater 2005, 4, 138–142. [PubMed: 15640806]

[50]. Zhang MX; Yue JY; Cui R; Ma ZR; Wan H; Wang FF; Zhu SJ; Zhou Y; Kuang Y; Zhong YT et al. Bright quantum dots emitting at ~ 1,600 nm in the NIR-IIb window for deep tissue fluorescence imaging. Proc. Natl. Acad. Sci. USA 2018, 115, 6590–6595. [PubMed: 29891702]

[51]. Franke D; Harris DK; Chen O; Bruns OT; Carr JA; Wilson MWB; Bawendi MG Continuous injection synthesis of indium arsenide quantum dots emissive in the short-wavelength infrared. Nat. Commun 2016, 7, 12749. [PubMed: 27834371]

[52]. Zhong YT; Ma ZR; Zhu SJ; Yue JY; Zhang MX; Antaris AL; Yuan J; Cui R; Wan H; Zhou Y et al. Boosting the down-shifting luminescence of rare-earth nanocrystals for biological imaging beyond 1,500 nm. Nat. Commun 2017, 8, 737. [PubMed: 28963467]

[53]. Dang XG; Gu L; Qi JF; Correa S; Zhang GR; Belcher AM; Hammond PT Layer-by-layer assembled fluorescent probes in the second near-infrared window for systemic delivery and detection of ovarian cancer. Proc. Natl. Acad. Sci. USA 2016, 113, 5179–5184. [PubMed: 27114520]

[54]. Su QQ; Han SY; Xie XJ; Zhu HM; Chen HY; Chen CK; Liu RS; Chen XY; Wang F; Liu XG The effect of surface coating on energy migration-mediated upconversion. J. Am. Chem. Soc 2012, 134, 20849–20857. [PubMed: 23210614]

[55]. Wang F; Liu XG Upconversion multicolor fine-tuning: Visible to near-infrared emission from lanthanide-doped $NaYF_4$ nanoparticles. J. Am. Chem. Soc 2008, 130, 5642–5643. [PubMed: 18393419]

[56]. Li DG; Qin WP; Zhang P; Wang LL; Lan M; Shi PB Efficient luminescence enhancement of Gd_2O_3: Ln^{3+} (Ln = Yb/Er, Eu) NCs by codoping Zn^{2+} and Li^+ inert ions. Opt. Mater. Express 2017, 7, 329–340.

[57]. Rahman P; Green M The synthesis of rare earthfluoride based nanoparticles. Nanoscale 2009, 1, 214–224. [PubMed: 20644840]

[58]. Wang X; Zhuang J; Peng Q; Li YD Hydrothermal synthesis of rare-earth fluoride nanocrystals. Inorg. Chem 2006, 45, 6661–6665. [PubMed: 16903720]

[59]. Yin WY; Zhao LN; Zhou LJ; Gu ZJ; Liu XX; Tian G; Jin S; Yan L; Ren WL; Xing GM et al. Enhanced red emission from GdF_3: Yb^{3+}, Er^{3+} upconversion nanocrystals by Li^+ doping and their application for bioimaging. Chem. –Eur. J 2012, 18, 9239–9245. [PubMed: 22729946]

[60]. Gu ZJ; Yan L; Tian G; Li SJ; Chai ZF; Zhao YL Recent advances in design and fabrication of upconversion nanoparticles and their safe theranostic applications. Adv. Mater 2013, 25, 3758–3779. [PubMed: 23813588]

[61]. Haase M; Schäfer H Upconverting nanoparticles. Angew. Chem., Int. Ed 2011, 50, 5808–5829.

[62]. Vetrone F; Naccache R; Mahalingam V; Morgan CG; Capobianco JA The active-core/active-shell approach: A strategy to enhance the upconversion luminescence in lanthanide-doped nanoparticles. Adv. Funct. Mater 2009, 19, 2924–2929.

[63]. Wang F; Deng RR; Wang J; Wang QX; Han Y; Zhu HM; Chen XY; Liu XG Tuning upconversion through energy migration in core–shell nanoparticles. Nat. Mater 2011, 10, 968–973. [PubMed: 22019945]

[64]. Wang F; Han Y; Lim CS; Lu YH; Wang J; Xu J; Chen HY; Zhang C; Hong MH; Liu XG Simultaneous phase and size control of upconversion nanocrystals through lanthanide doping. Nature 2010, 463, 1061–1065. [PubMed: 20182508]

[65]. Zhou J; Liu Z; Li FY Upconversion nanophosphors for small-animal imaging. Chem. Soc. Rev 2012, 41, 1323–1349. [PubMed: 22008740]

[66]. Dong H; Du SR; Zheng XY; Lyu GM; Sun LD; Li LD; Zhang PZ; Zhang C; Yan CH Lanthanide nanoparticles: From design toward bioimaging and therapy. Chem. Rev 2015, 115, 10725–10815. [PubMed: 26151155]

[67]. Huo LL; Zhou JJ; Wu RZ; Ren JF; Zhang SJ; Zhang JJ; Xu SQ Dual-functional β-$NaYF_4$: Yb^{3+}, Er^{3+} nanoparticles for bioimaging and temperature sensing. Opt. Mater. Express 2016, 6, 1056–1064.

[68]. Kenry; Duan YK; Liu B Recent advances of optical imaging in the second near-infrared window. Adv. Mater 2018, 30, 1802394.

[69]. Xue ZL; Zeng SJ; Hao JH Non-invasive through-skull brain vascular imaging and small tumor diagnosis based on NIR-II emissive lanthanide nanoprobes beyond 1,500 nm. Biomaterials 2018, 171, 153–163. [PubMed: 29689412]

[70]. You WW; Tu DT; Zheng W; Shang XY; Song XR; Zhou SY; Liu Y; Li RF; Chen XY Large-scale synthesis of uniform lanthanide-doped $NaREF_4$ upconversion/downshifting nanoprobes for bioapplications. Nanoscale 2018, 10, 11477–11484. [PubMed: 29888369]

[71]. Li YB; Zeng SJ; Hao JH Non-invasive optical guided tumor metastasis/vessel imaging by using lanthanide nanoprobe with enhanced down-shifting emission beyond 1,500 nm. ACS Nano 2019, 13, 248–259. [PubMed: 30604961]

[72]. Iyer AK; Khaled G; Fang J; Maeda H Exploiting the enhanced permeability and retention effect for tumor targeting. Drug Discov. Today 2006, 11, 812–818. [PubMed: 16935749]

[73]. Zhong YT; Rostami I; Wang ZH; Dai HJ; Hu ZY Energy migration engineering of bright rare-earth upconversion nanoparticles for excitation by light-emitting diodes. Adv. Mater 2015, 27, 6418–6422. [PubMed: 26393770]

[74]. Zhong YT; Tian G; Gu ZJ; Yang YJ; Gu L; Zhao YL; Ma Y; Yao JN Elimination of photon quenching by a transition layer to fabricate a quenching-shield sandwich structure for 800 nm excited upconversion luminescence of Nd^{3+}-sensitized nanoparticles. Adv. Mater 2014, 26, 2831–2837. [PubMed: 24338994]

[75]. Wang R; Li XM; Zhou L; Zhang F Epitaxial seeded growth of rare-earth nanocrystals with efficient 800 nm near-infrared to 1,525 nm short-wavelength infrared downconversion photoluminescence for *in vivo* bioimaging. Angew. Chem., Int. Ed 2014, 53, 12086–12090.

[76]. Weissleder R A clearer vision for *in vivo* imaging. Nat. Biotechnol 2001, 19, 316–317. [PubMed: 11283581]

[77]. Fan Y; Wang PY; Lu YQ; Wang R; Zhou L; Zheng XL; Li XM; Piper JA; Zhang F Lifetime-engineered NIR-II nanoparticles unlock multiplexed *in vivo* imaging. Nat. Nanotechnol 2018, 13, 941–946. [PubMed: 30082923]

[78]. He S; Johnson NJJ; Nguyen Huu VA; Cory E; Huang YR; Sah RL; Jokerst JV; Almutairi A Simultaneous enhancement of photoluminescence, MRI relaxivity, and CT contrast by tuning the interfacial layer of lanthanide heteroepitaxial nanoparticles. Nano Lett. 2017, 17, 4873–4880. [PubMed: 28657755]

[79]. Liu L; Li XM; Fan Y; Wang CY; El-Toni AM; Alhoshan MS; Zhao DY; Zhang F Elemental migration in core/shell structured lanthanide doped nanoparticles. Chem. Mater 2019, 31, 5608–5615.

[80]. Johnson NJJ; He S; Diao S; Chan EM; Dai HJ; Almutairi A Direct evidence for coupled surface and concentration quenching dynamics in lanthanide-doped nanocrystals. J. Am. Chem. Soc 2017, 139, 3275–3282. [PubMed: 28169535]

[81]. Liu YF; Zhao J; Zhang Y; Zhang HF; Zhang ZL; Gao HP; Mao YL Enhanced single-band red upconversion luminescence of α-$NaErF_4$: Mn nanoparticles by a novel hollow-shell structure under multiple wavelength excitation. J. Alloys Compd 2019, 810, 151761.

[82]. Wang X; Yakovliev A; Ohulchanskyy TY; Wu LN; Zeng SJ; Han XJ; Qu JL; Chen GY Efficient erbium-sensitized core/shell nanocrystals for short wave infrared bioimaging. Adv. Opt. Mater 2018, 6, 1800690.

[83]. Fields RA; Birnbaum M; Fincher CL Highly efficient Nd: YVO_4 diode-laser end-pumped laser. Appl. Phys. Lett 1987, 51, 1885–1886.

[84]. Kane TJ; Byer RL Monolithic, unidirectional single-mode Nd: YAG ring laser. Opt. Lett 1985, 10, 65–67. [PubMed: 19724347]

[85]. Ren F; Ding LH; Liu HH; Huang Q; Zhang H; Zhang LJ; Zeng JF; Sun Q; Li Z; Gao MY Ultra-small nanocluster mediated synthesis of Nd^{3+}-doped core-shell nanocrystals with emission in the second near-infrared window for multimodal imaging of tumor vasculature. Biomaterials 2018, 175, 30–43. [PubMed: 29800756]

[86]. Dai Y; Yang DP; Yu DP; Cao C; Wang QH; Xie SH; Shen L; Feng W; Li FY Mussel-inspired polydopamine-coated lanthanide nanoparticles for NIR-II/CT dual imaging and photothermal therapy. ACS Appl. Mater. Interfaces 2017, 9, 26674–26683. [PubMed: 28726368]

[87]. Quintanilla M; Zhang Y; Liz-Marzán LM Subtissue plasmonic heating monitored with CaF_2: Nd^{3+}, Y^{3+} nanothermometers in the second biological window. Chem. Mater 2018, 30, 2819–2828.

[88]. Villa I; Vedda A; Cantarelli IX; Pedroni M; Piccinelli F; Bettinelli M; Speghini A; Quintanilla M; Vetrone F; Rocha U et al. 1.3 μm emitting SrF_2: Nd^{3+} nanoparticles for high contrast *in vivo* imaging in the second biological window. Nano Res. 2015, 8, 649–665.

[89]. Rocha U; Kumar KU; Jacinto C; Villa I; Sanz-Rodríguez F; del Carmen Iglesias de la Cruz M; Juarranz A; Carrasco E; van Veggel FCJM; Bovero E et al. Neodymium-doped LaF_3 nanoparticles for fluorescence bioimaging in the second biological window. Small 2014, 10, 1141–1154. [PubMed: 24123958]

[90]. Qin QS; Zhang PZ; Sun LD; Shi S; Chen NX; Dong H; Zheng XY; Li LM; Yan CH Ultralow-power near-infrared excited neodymium-doped nanoparticles for long-term *in vivo* bioimaging. Nanoscale 2017, 9, 4660–4664. [PubMed: 28345715]

[91]. Jiang XY; Cao C; Feng W; Li FY Nd^{3+}-doped $LiYF_4$ nanocrystals for bio-imaging in the second near-infrared window. J. Mater. Chem. B 2016, 4, 87–95. [PubMed: 32262811]

[92]. Zhao MY; Wang R; Li BH; Fan Y; Wu YF; Zhu XY; Zhang F Precise *in vivo* inflammation imaging using *in situ* responsive cross-linking of glutathione-modified ultra-small NIR-II lanthanide nanoparticles. Angew. Chem 2019, 131, 2072–2076.

[93]. Li XL; Jiang MY; Li YB; Xue ZL; Zeng SJ; Liu HR 808 nm laser-triggered NIR-II emissive rare-earth nanoprobes for small tumor detection and blood vessel imaging. Mater. Sci. Eng. C 2019, 100, 260–268.

[94]. Xue XJ; Duan ZC; Suzuki T; Tiwari RN; Yoshimura M; Ohishi Y Luminescence properties of α-$NaYF_4$: Nd^{3+} nanocrystals dispersed in liquid: Local field effect investigation. J. Phys. Chem. C 2012, 116, 22545–22551.

[95]. Zhou JJ; Shirahata N; Sun HT; Ghosh B; Ogawara M; Teng Y; Zhou SF; Sa Chu RG; Fujii M; Qiu JR Efficient dual-modal NIR-to-NIR emission of rare earth ions co-doped nanocrystals for biological fluorescence imaging. J. Phys. Chem. Lett 2013, 4, 402–408. [PubMed: 26281731]

[96]. Chen GY; Ohulchanskyy TY; Liu S; Law WC; Wu F; Swihart MT; Ågren H; Prasad PN Core/shell $NaGdF_4$: Nd^{3+}/$NaGdF_4$ nanocrystals with efficient near-infrared to near-infrared downconversion photoluminescence for bioimaging applications. ACS Nano 2012, 6, 2969–2977. [PubMed: 22401578]

[97]. Wang R; Zhou L; Wang WX; Li XM; Zhang F *In vivo* gastrointestinal drug-release monitoring through second near-infrared window fluorescent bioimaging with orally delivered microcarriers. Nat. Commun 2017, 8, 14702. [PubMed: 28281530]

[98]. Crosby GA; Whan RE; Alire RM Intramolecular energy transfer in rare earth chelates. role of the triplet state. J. Chem. Phys 1961, 34, 743–748.

[99]. Crosby GA; Whan RE; Freeman JJ Spectroscopic studies of rare earth chelates. J. Phys. Chem 1962, 66, 2493–2499.

[100]. Hofstraat JW; Wolbers MPO; van Veggel FCJM; Reinhoudt DN; Werts MHV; Verhoeven JW Near-IR luminescent rare earth ion-sensitizer complexes. J. Fluoresc 1998, 8, 301–308.

[101]. Li YB; Li XL; Xue ZL; Jiang MY; Zeng SJ; Hao JH Second near-infrared emissive lanthanide complex for fast renal-clearable *in vivo* optical bioimaging and tiny tumor detection. Biomaterials 2018, 169, 35–44. [PubMed: 29631166]

[102]. Gu YY; Guo ZY; Yuan W; Kong MY; Liu YL; Liu YT; Gao YL; Feng W; Wang F; Zhou JJ et al. High-sensitivity imaging of time-domain near-infrared light transducer. Nat. Photonics 2019, 13, 525–531.

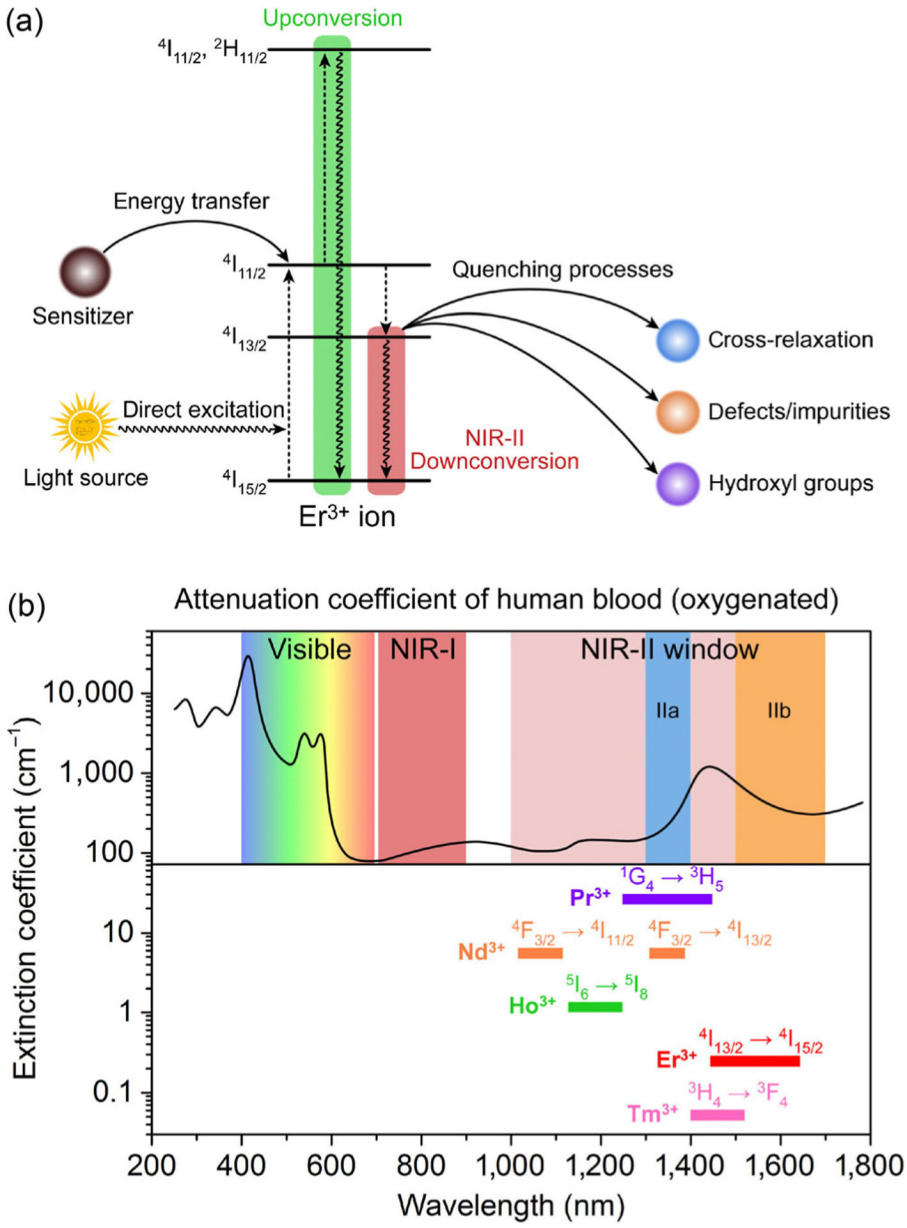

Figure 1.

(a) Simplified energy-level diagrams depicting the luminescence mechanism of Er^{3+} ion. (b) Attenuation coefficient of human blood (oxygenated) in the 300–1,700 nm spectral range. The spectral extensions of visible, NIR-I, and NIR-II (including NIR-IIa and NIR-IIb) imaging windows are schematically indicated. The emission spectral ranges of the different lanthanide ions are also included.

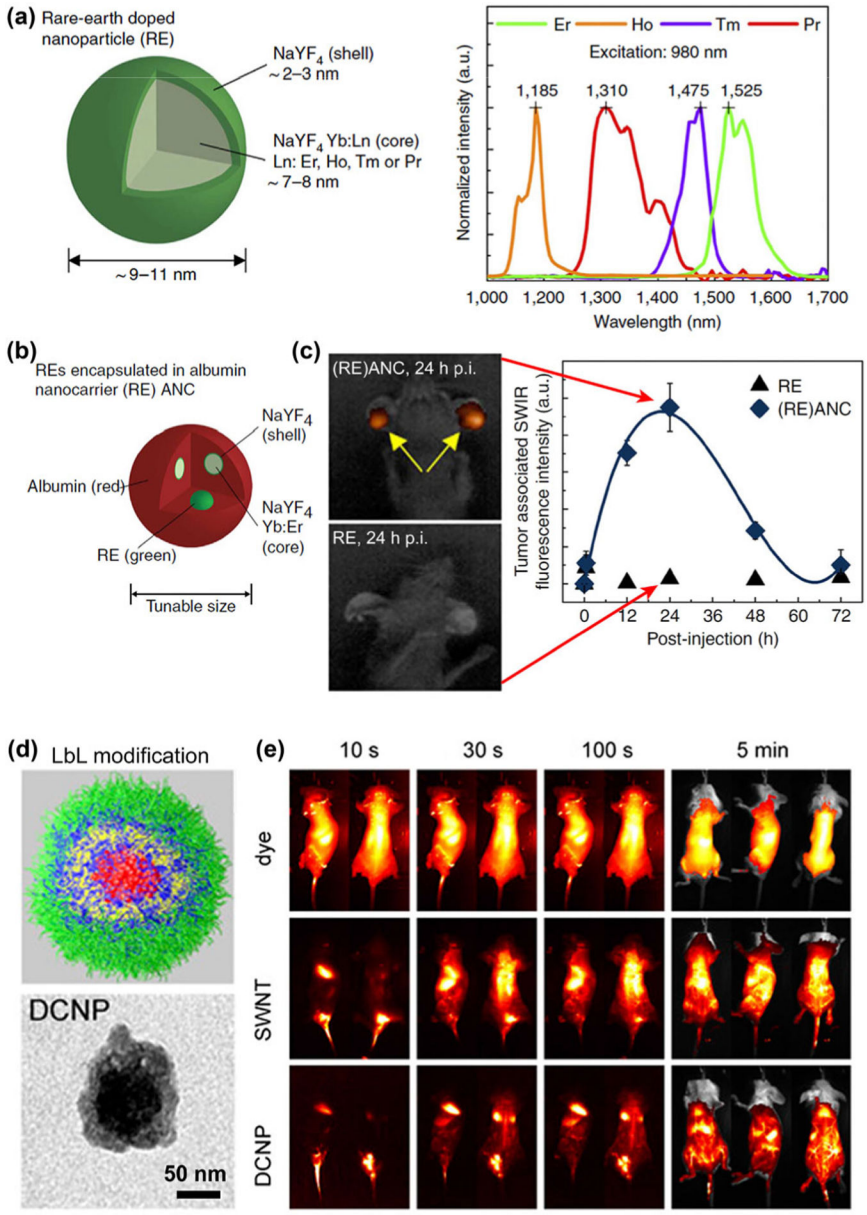

Figure 2.

(a) Properties of the RE doped nanoprobes. The RE nanoprobes consist of a $NaYF_4$ Yb:Ln-doped core (Ln: Er, Ho, Tm or Pr) surrounded by an undoped shell of $NaYF_4$. The emission of Er-doped nanoprobes is centered at 1,525 nm in the NIR-IIb window. (b) RE encapsulated albumin nanocarriers ((RE)ANC) consist of RE nanoprobes encapsulated by a coating of human serum albumin (HSA) to form an inorganic-organic nanocomposite. (c) Tumor accumulation over time of REs and (RE)ANCs in the ears of transgenic mice after intraperitoneally injection. Reproduced with permission from Ref. [18], © Nature Publishing Group 2013. (d) Illustration of spherical LbL modified RE NIR-IIb probes and corresponding TEM image. (e) Whole-body NIR-II images at time points from 10 s to 5 min post-injection of organic dye (excitation: 808 nm; emission peak: 1,100 nm), single-walled carbon nanotubes (SWNT; excitation: 808 nm; emission peak: 1,225 nm) and RE NIR-IIb

probes (DCNP; excitation: 980 nm; emission peak: 1,575 nm). Reproduced with permission from Ref. [53], © National Academy of Sciences 2016.

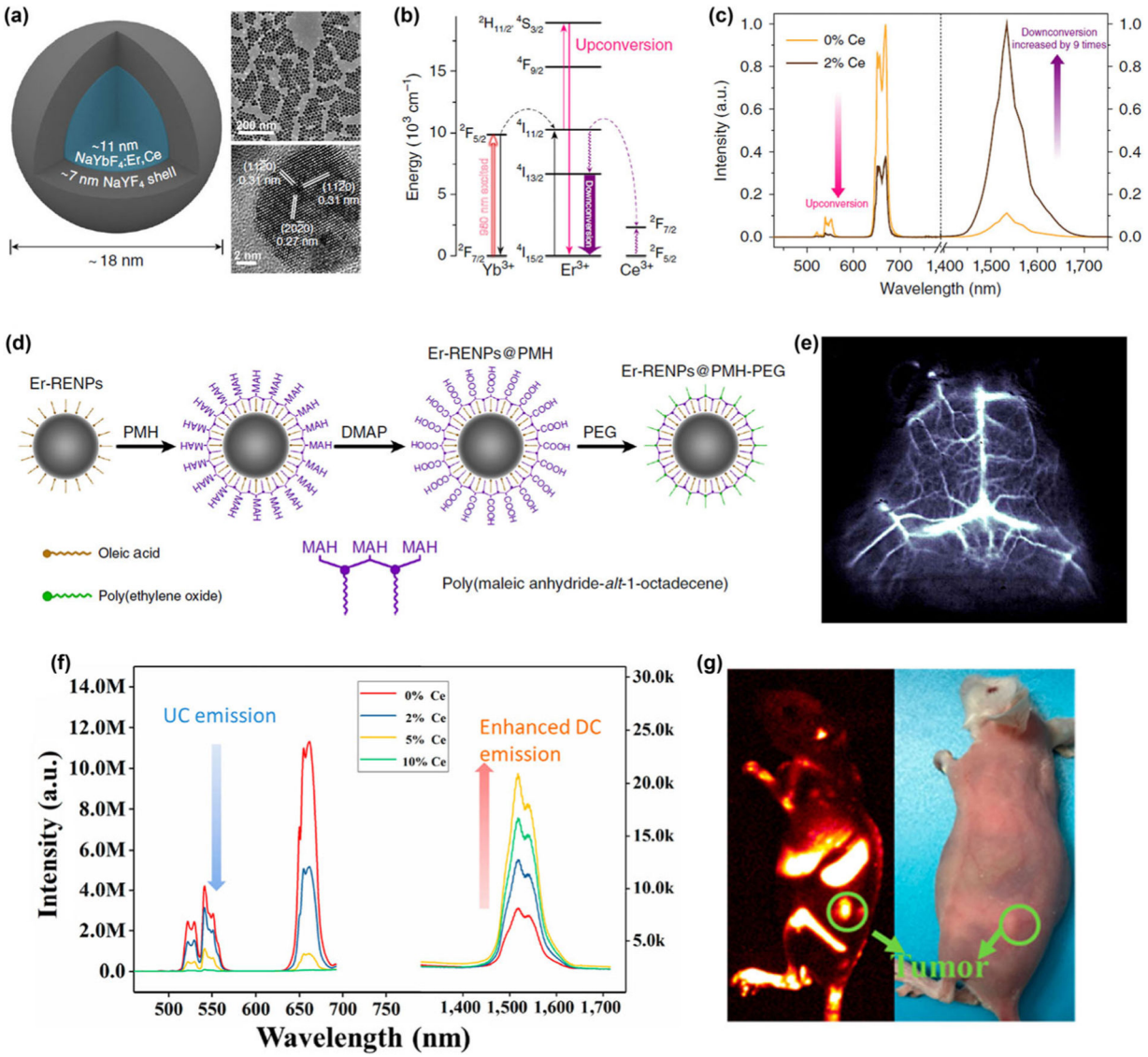

Figure 3.

(a) Schematic design of a $NaYbF_4$:Er,Ce@$NaYF_4$ core-shell nanoparticle (left) with corresponding large scale TEM image (upper right) and HRTEM image (lower right). (b) Simplified energy-level diagrams depicting the energy transfer between Yb^{3+}, Er^{3+}, and Ce^{3+} ions. (c) Upconversion and down-conversion luminescence spectra of the ErNPs with 0 and 2% Ce^{3+} doping. (d) Schematic illustration outlining the PMH coating and PEGylation procedure for the ErNPs. (e) Cerebral vascular image (exposure time: 20 ms) in NIR-IIb region by intravenous injection of ErNPs. Reproduced with permission from Ref. [52], © Zhong, Y. T. et al. 2017. (f) Upconversion and NIR-IIb down-conversion luminescence spectra of $NaLuF_4$:Gd/Yb/Er nanorods doped with different contents of Ce^{3+} (0, 2 mol%, 5 mol%, 10 mol%). (g) Digital photograph (right) of tumor-bearing mouse and *in vivo* NIR-IIb luminescence imaging (left) of the tumor-bearing mouse (the green circle indicated the tumor site) by intravenous injection of $NaLuF_4$:Gd/Yb/Er/Ce. Reproduced with permission from Ref. [71], © American Chemical Society 2019.

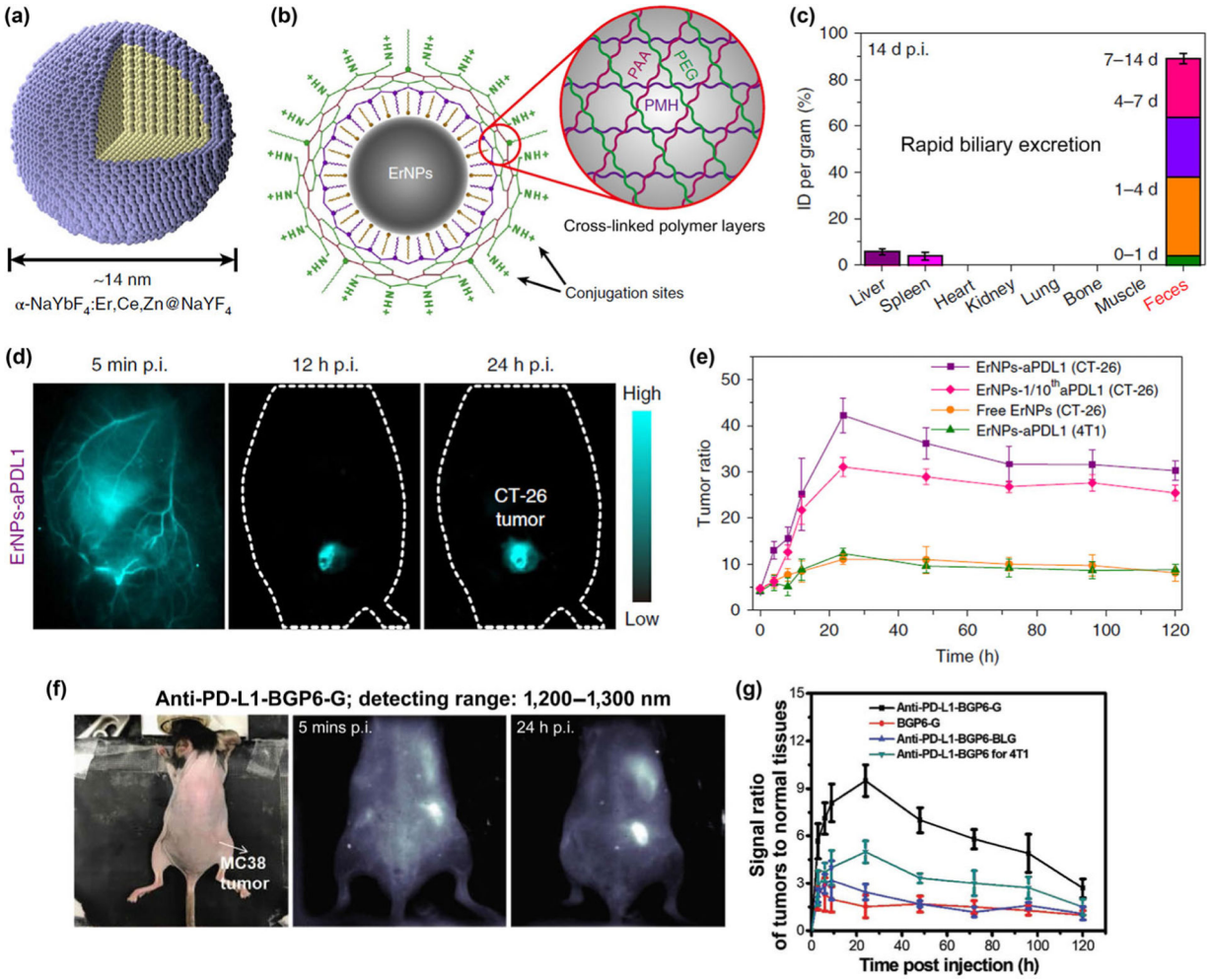

Figure 4.

(a) Schematic design of core-shell Zn-doped α-ErNPs. (b) Schematic illustration of the hydrophilic ErNPs with cross-linking polymeric layers and amine groups on the surface as conjugation sites. (c) Bio-distribution of ErNPs in main organs and feces of ErNP-treated mice at 14-d post-injection, indicating the rapid biliary excretion of the intravenously injected ErNPs. (d) The wide-field NIR-IIb images of CT-26 tumor mice treated with ErNPs-aPDL1 at time points from 5 min to 24 h post-injection. (e) Corresponding T/NT ratios of ErNPs in tumor were plotted as a function of time. Reproduced with permission from Ref. [32], © Nature Publishing Group 2019. (f) The wide-field NIR-II images (detecting range: 1,200–1,300 nm) of MC38 tumor mice treated with anti-PD-L1-BGP6-G (BGP6-G is an organic dye emitting in the NIR-II range) at time points from 5 min to 24 h post-injection. (g) Corresponding T/NT ratios of BGP6-G in tumor were plotted as a function of time. Reproduced with permission from Ref. [26], © Wiley 2018.

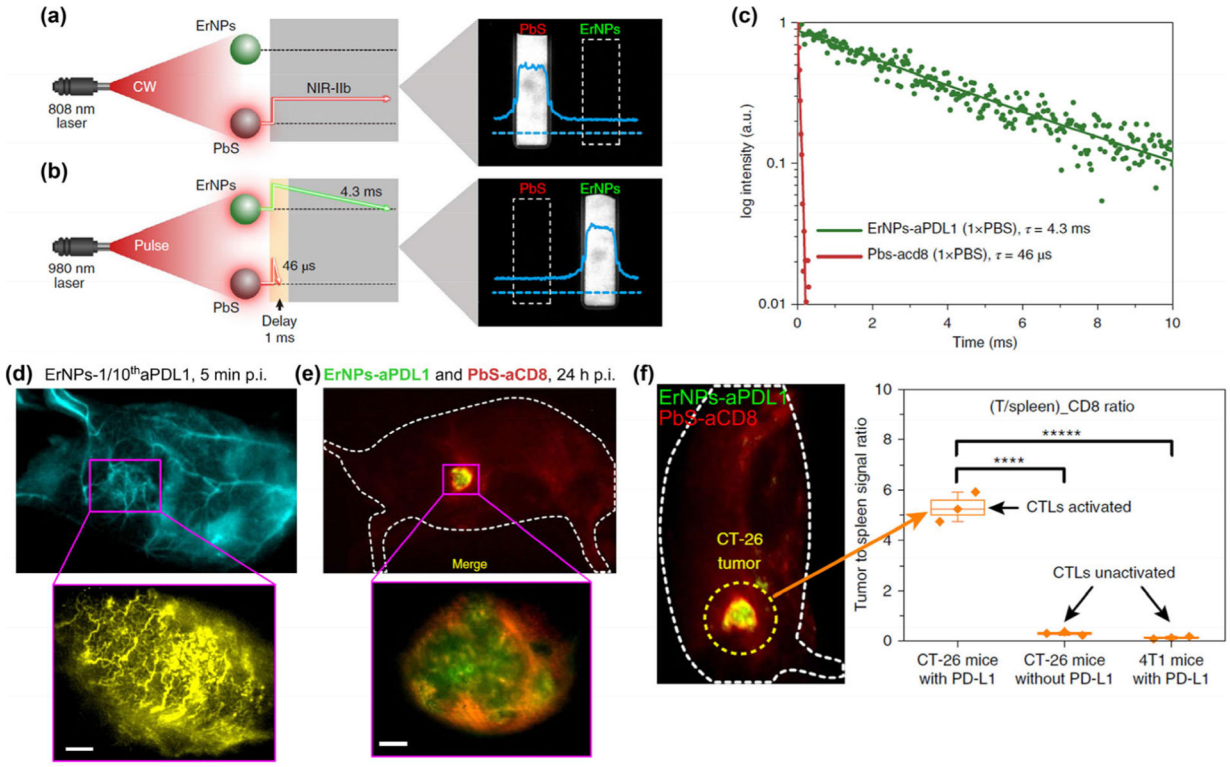

Figure 5.

(a) Schematic illustration outlining the experimental setup (left) to distinguish the PbS QD emission channel (right) by using an 808 nm continuous wave (CW) laser. (b) Schematic of the experimental setup (left) to differentiate the long-lived ErNP luminescence (right) from short-lived PbS QD fluorescence by using a 980 nm laser pulse. The insets show corresponding cross-sectional intensity profiles (blue color). (c) Lifetime decays of ErNPs-aPDL1 and PbS-aCD8 in 1xPBS solution. (d) The wide-field images (upper) of a CT-26 tumor mouse treated with ErNPs-1/10thaPDL1 containing 20 µg anti-PD-L1 mAb (1 mg/kg), and corresponding high-magnification molecular imaging (lower) of the CT-26 tumor at 5 min post injection of ErNPs-1/10thaPDL1 (scale bar, 500 µm). (e) Two-plex molecular imaging (upper) of a CT-26 tumor mouse at 24 h post intravenous injection of mixed ErNPs-aPDL1 (green color) and PbS-aCD8 (red color). The zoomed-in high-magnification two-plex image (lower) outlines the CT-26 tumor with micrometer image resolution (scale bar, 500 µm). (f) Wide-field image reveals the *in vivo* bio-distributions of ErNPs-aPDL1 and PbS-aCD8 in a CT-26 tumor mouse intravenously injected with mixed ErNPs-aPDL1 and PbS-aCD8, and corresponding (T/spleen)_CD8 ratios. Reproduced with permission from Ref. [32], © Nature Publishing Group 2019.

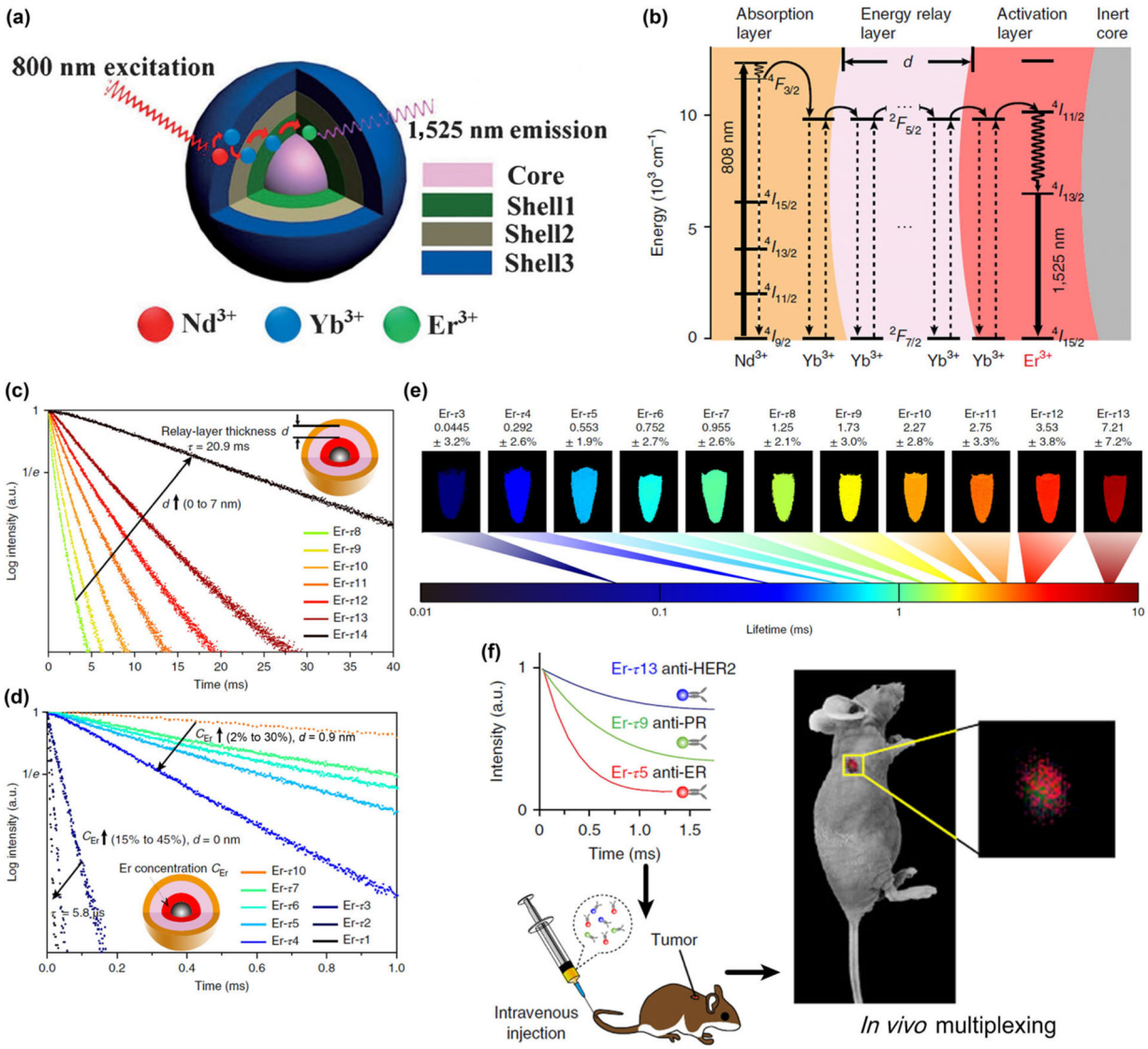

Figure 6.

(a) Structure of the $NaGdF_4/Na(Gd,Yb)F_4$:Er/$NaYF_4$:Yb/$NaNdF_4$:Yb nanocrystal for NIR-IIb luminescence. Reproduced with permission from Ref. [75], © Wiley 2018. (b) Energy level diagram illustrating the luminescence process of the Nd sensitized core-multi-shell nanoparticles. (c) Luminescence decay curves measured at 1,525 nm from the as-prepared Er nanoparticles with energy relay shells of increasing thickness *d* from 0 to 7 nm (identical composition). (d) Luminescence decay curves of the nanoparticles with incremental Er^{3+} doping concentration CEr from 2% to 30% for *d* = 0.9 nm and from 15% to 45% for *d* = 0 nm. (e) Pseudocolour-mapped lifetime images of the Er nanoparticles contained in centrifuge tubes acquired by the time-resolved NIR-II imaging system. (f) Schematics illustrating animal experiment procedures. Three batches of Er nanoparticles exhibiting distinct lifetimes are conjugated to three antibodies (anti-ER, anti-PR and anti-HER2), respectively, and intravenously injected into the mouse via tail vein. Lifetime-resolved

imaging is then performed to quantify the biomarker expressions on the tumor. Reproduced with permission from Ref. [77], © Springer Nature 2018.

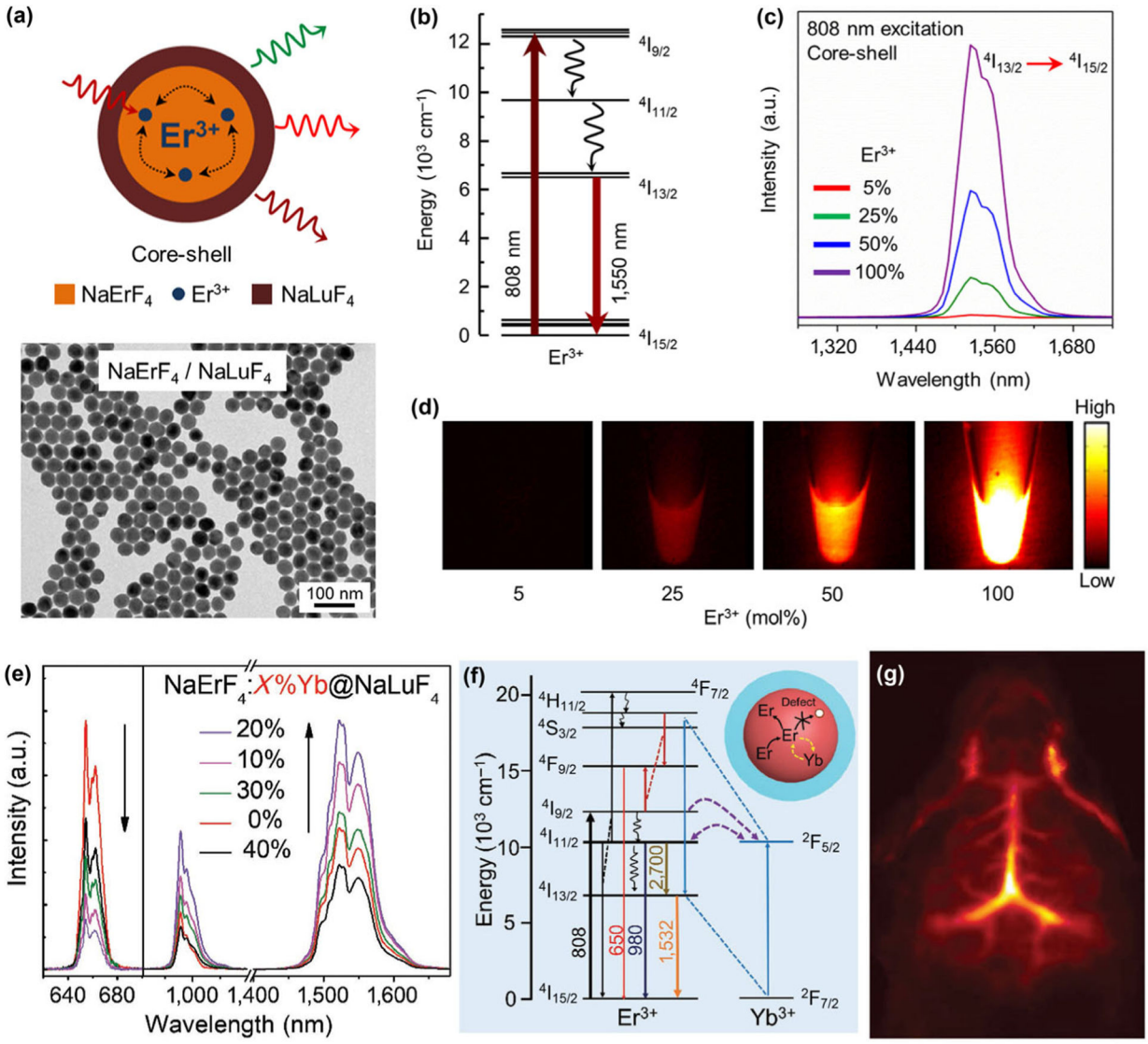

Figure 7.

(a) Schematic illustration of the NaErF4-NaLuF4 core-shell nanocrystals structural composition, and corresponding TEM image. (b) Energy level diagram of Er^{3+} showing the excitation (808 nm) and the down-conversion emission (1,550 nm) levels. (c) Emission spectra of the core-shell nanocrystals with variable Er^{3+} dopant concentrations in the core showing down-conversion NIR-IIb emission under 808 nm excitation. (d) Down-conversion emission images from colloidal dispersion of core-shell nanocrystals shows emission enhancement with increase in Er^{3+} dopant concentration. Reproduced with permission from Ref. [80], © American Chemical Society 2017. (e) Upconversion and down-conversion luminescence spectra demonstrate the doping of Yb^{3+} into the core of core–shell $NaErF_4$:*x* %Yb^{3+}@$NaLuF_4$ (*x* = 10, 20, 30, 40) nanocrystals for enhanced NIR-IIb luminescence. (f) Simplified energy level diagrams of Er^{3+} and Yb^{3+} ions depicting the emitting and energy transfer processes. (g) *In vivo* NIR-IIb brain vasculature imaging through tail vein injection

of PAA-coated $NaErF_4:Yb^{3+}20\%@NaLuF_4$ core/shell nanocrystals. Reproduced with permission from Ref. [82], © Wiley 2018.

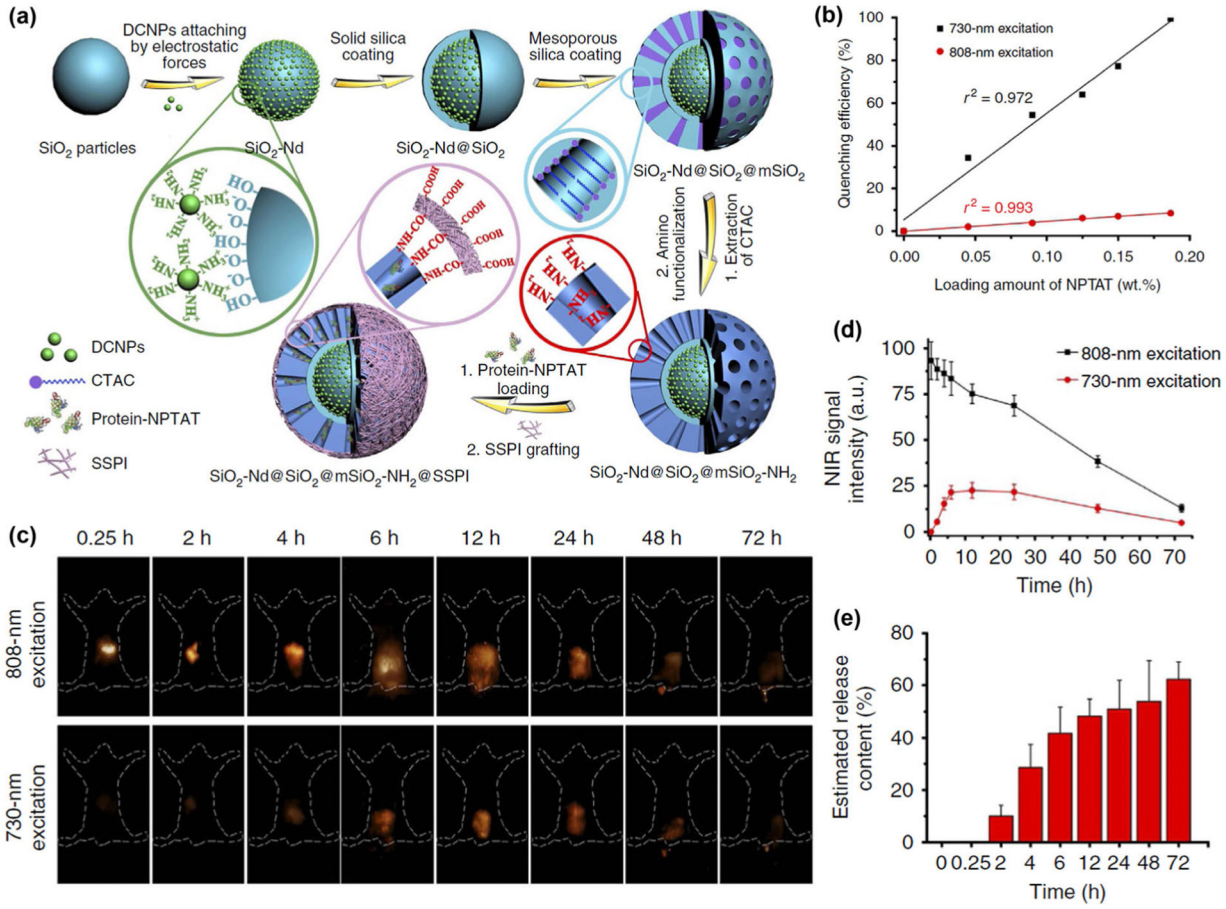

Figure 8.

(a) Procedures of NIR-II luminescent mesoporous microcarriers preparation and protein drugs loading. (b) NIR-II luminescence intensity of microcarriers loaded with different amounts of NPTAT under 730- or 808-nm excitation, respectively. (c) NIR-II bio-imaging of mice at different times after orally gavaging protein-NPTAT-loaded microcarriers under 730- or 808-nm excitation. (d) Corresponding signal intensity curves. (e) Corresponding *in vivo* release percentages of protein-NPTAT from microcarriers. Reproduced with permission from Ref. [97], © Wang, R. et al. 2017.

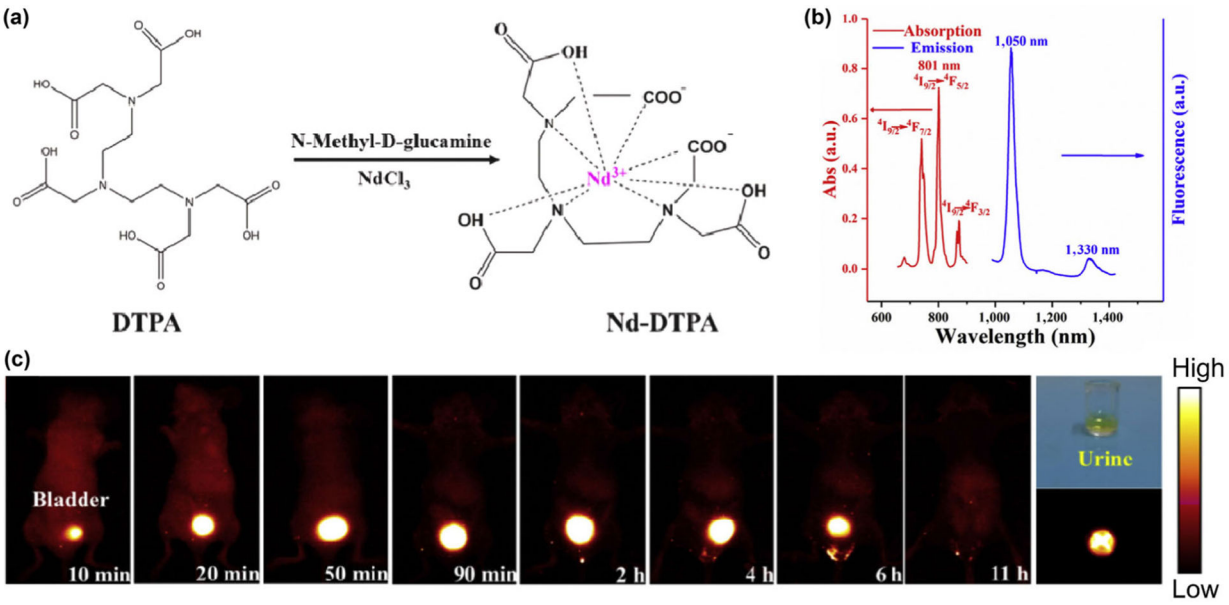

Figure 9.

(a) Schematic illustration of the molecular structure of the DTPA and Nd-DTPA, along with the synthesis process of Nd-DTPA. (b) UV–vis absorption spectrum (600–900 nm) and photoluminescent spectrum of the Nd-DTPA complex under the excitation of 808 nm laser, demonstrating the efficient narrow-band emissions centered at 1,050 and 1,330 nm. (c) NIR-II imaging of the mouse in the supine position, revealing the rapid excretion of Nd-DTPA molecule via kidney. The digital photograph (upper-right end) and the NIR-II imaging (lower-right end) of the urine sample are also collected after 2 h post-injection. Reproduced with permission from Ref. [101], © Elsevier Ltd 2018.